Contents lists available at ScienceDirect

Tectonophysics

journal homepage: www.elsevier.com/locate/tecto

Migration of hot to super-hot palaeo-fluids in an extensional setting (eastern Elba Island, Italy)

Martina Zucchi [a,*], Andrea Brogi [a,b], Domenico Liotta [a,b], Rosa Anna Fregola [a], Alfredo Caggianelli [a], Gennaro Ventruti [a], Riccardo Avanzinelli [c], Giovanni Ruggieri [d]

[a] *University of Bari, Department of Earth and Geoenvironmental Sciences, Bari, Italy*
[b] *National Research Council – Institute of Geoscience and Earth Resources (IGG-CNR), Pisa, Italy*
[c] *University of Florence, Department of Earth Sciences, Florence, Italy*
[d] *National Research Council – Institute of Geoscience and Earth Resources (IGG-CNR), Florence, Italy*

ARTICLE INFO

Keywords:
Extensional tectonics
Hydrothermal mineralisation
Exhumed geothermal system
Fluid inclusions
Magmatic fluids

ABSTRACT

Understanding how hot (250°–350 °C) to super-hot (>350 °C) fluids circulate and interact with host rocks in fault-controlled upper continental crust is a challenging task. In this paper, we present the results of a structural, fluid inclusions, Sr isotope, petrographic and mineral study on an exhumed geothermal system to describe how hot to super-hot fluids were controlled by the increased permeability resulting from the interplay between low-angle normal faults and high-angle oblique-slip faults, the latter being part of a regional transfer zone. The study area is located on the eastern Elba Island (northern Tyrrhenian Sea, Italy), where the emplacement of a Messinian felsic intrusion has allowed hydrothermal fluids to circulate in relation to a fault-related permeability of the order of 10^{-15} to 10^{-13} m^2. Magmatic fluids reacted with the host rocks (carbonate and phyllite) to form Fe-ore deposits hosted within the fault zones that controlled the fluid flow. Fluid inclusions trapped in quartz crystals indicate that the fluids consisted of saline solutions (salinity from 18.0 to 26.6 wt% NaCl eq.), which later mixed with low salinity waters of probably meteoric origin. The fluid temperature during the main hydrothermal stage ranged between about 300° and 360 °C under an estimated maximum hydrostatic pressure of 28–30 MPa. In contrast, the maximum possible temperature was about 400 °C at a lithostatic pressure of 89 MPa. The hydraulic breccias formed as a result of the transient fluid pressurisation up to lithostatic values, due to the self-sealing process and the subsequent pressure drop, down to hydrostatic values, as framed in the hydrofracturing processes. The results provide useful inputs for the identification of geothermal and ore-body targets in those geological settings where fluids of magmatic and meteoric origin are controlled by active faults in an extensional tectonic regime.

1. Introduction

Migration and storage of geothermal fluids in the upper crust are mostly controlled by permeable rock volumes corresponding to crustal sectors affected by brittle deformation (Curewitz and Karson, 1997; Rowland and Sibson, 2004; Liotta et al., 2010; Pérez-Flores et al., 2016; Brogi et al., 2021), especially in extensional tectonic settings with coeval magmatic activity (Chmielowski et al., 1999; Alaniz-Álvarez et al., 2002; Creixell et al., 2006; Liotta and Brogi, 2020).

Indeed, magmatic bodies emplaced at shallow crustal levels (4–8 km) induce thermal perturbations in the host rocks and promote the circulation of large volumes of hot (250°–350 °C) or super-hot (>350 °C) fluids of magmatic, metamorphic and/or meteoric origin (Nabelek and Labotka, 1993; Heinrich et al., 1995; Gianelli and Ruggieri, 2002; Boiron et al., 2007; Rossetti et al., 2007; Pope et al., 2014, 2016; Ármannsson et al., 2015; Ducoux et al., 2017; Zucchi et al., 2017).

In these tectonic settings, crustal stretching is accompanied by normal faults and transfer zones, the latter separating crustal volumes subjected to different deformation although resulting in the same finite elongation (Lister et al., 1986; Gibbs, 1990; Liotta, 1991; Liotta et al., 2015). The intersection of normal and transfer faults results in the genesis of zones where deformation and secondary permeability are enhanced (Curewitz and Karson, 1997; Acocella and Funiciello, 2006; Rowland and Sibson, 2004; Liotta et al., 2021), promoting the

---

* Corresponding author.
E-mail address: martina.zucchi@uniba.it (M. Zucchi).

https://doi.org/10.1016/j.tecto.2024.230210
Received 15 May 2023; Received in revised form 10 January 2024; Accepted 11 January 2024

development of local reservoirs, as documented in several geothermal systems, either active (Brhun et al., 1987; Yano and Ishido, 1996; Brogi, 2004; Rowland and Sibson, 2004; Monastero et al., 2005; Faulds et al., 2012; Alçiçek et al., 2018; Liotta and Brogi, 2020; Matera et al., 2021) or exhumed (Hedenquist and Lowenstern, 1994; Brogi and Fulignati, 2012; Liotta et al., 2020; Zucchi et al., 2017; Matera et al., 2021). Predicting fracture distribution and permeability variation at depth, especially for targets in the depth range 2000–4000 m b.g.l., is a challenging task in geothermal exploration, since reservoir potential estimation becomes crucial for planning sustainable resource exploitation. Furthermore, reservoir permeability is transient and controlled by the interplay between tectonic activity (which enhances permeability) and fracture sealing caused by precipitation of mineral phases from saline fluids (Sibson, 1987; Cox, 1999; Uysal et al., 2009; Alt-Epping et al., 2013). As a result, permeability evaluation can be confidently measured only after drilling or, differently, estimated through indirect analyses (e.g., geophysical surveys or numerical simulations), that usually provides values with a large margin of uncertainty.

Alternatively, useful information on hydraulic parameters, usually obtained after drilling, can be obtained by studying analogue fossil and exhumed geothermal systems, where the distribution of the hydrothermal mineral veins, as well as their development in terms of relative chronology and texture, can reveal the permeability evolution of the fracture network that hosted the parent geothermal fluids at the time and depth of the fluid flow (Gillespie et al., 1999).

In this view, we present a structural, minero-petrographic, fluid inclusion and Sr isotopic study of a sector of eastern Elba Island (Fig. 1), where the fracture network of damaged rock volumes channelled hot geothermal fluids of magmatic origin that deposited Fe-oxides and Fe-hydroxides during the cooling of the Late Messinian Porto Azzurro monzogranite (Spiess et al., 2021). In particular hematite/magnetite veins, exploited in the 1960s and 1970s in the Reale-Terranera mining district (Fig. 1b) cut a magnesian Fe-skarn deposit, recently studied by Garofalo et al. (2023). The study area was selected because it clearly shows the effects on the permeability evolution caused by the interaction of two different fault systems, well-described in the literature (e.g., Liotta et al., 2015; Zucchi et al., 2017; Spiess et al., 2021; Zucchi et al., 2022), involving the low-angle Zuccale Fault (Pertusati et al., 1993; Collettini and Holdsworth, 2004; Smith et al., 2007; Collettini et al., 2009) and the Capoliveri-Porto Azzurro transfer zone (Liotta et al., 2015, 2021; Spiess et al., 2022).

The main results provide useful inputs for the identification of geothermal targets in geological settings where geothermal fluids of magmatic and meteoric origin are controlled by active faults in an extensional tectonic setting, such as, for example, the Larderello geothermal area, in southern Tuscany (Fig. 1a).

2. Geological outline

Elba Island (Fig. 1a) is part of the inner zone of the Northern Apennines, an Alpine belt developed between the Cretaceous and Early Miocene by the convergence and collision of the African and European plates (Carmignani et al., 1994; Molli, 2008; Vai and Martini, 2001). Since the Early-Middle Miocene, the inner zone of the Northern Apennines has been affected by extension (Baldi et al., 1994; Carmignani et al., 1995; Brogi and Liotta, 2008; Barchi, 2010). The clearest evidence is the opening of the Tyrrhenian Basin (Bartole, 1995) and the thinning of the continental crust and lithosphere down to the present values of about 17–24 and 30–50 km thick, respectively (Calcagnile and Panza, 1981; Locardi and Nicolich, 1992; Cassinis et al., 2003; Moeller et al., 2013).

Elba Island, now located near the coast of Tuscany (Fig. 1a), is characterised by exhumed units that were partially involved in Late Oligocene-Early Miocene subduction (Bianco et al., 2015, 2019; Papeschi et al., 2020; Ryan et al., 2021). Furthermore, at least since the Langhian, widespread hybrid magmatism (i.e., resulting from mixing of crustal and mantle sources; Serri et al., 1993; Peccerillo, 2003) progressively took place from Corsica to Tuscany, following the eastward migration of extensional tectonics (Fig. 1a). In this context, the Tuscan archipelago (Fig. 1) and southern Tuscany experienced magmatic events during the Tortonian-Late Messinian time interval (e.g., Westerman et al., 2004; Dini et al., 2005; Rocchi et al., 2010; Caggianelli et al., 2014, 2018), defining an intense hydrothermal fluid circulation (e.g., Dini, 2003; Liotta et al., 2010; Vezzoni et al., 2016; Zucchi et al., 2017; Zucchi, 2020) that locally produced ore deposits that were extensively exploited from the Etruscan times until the 1980s.

Two main magmatic complexes are exposed on Elba Island. These were emplaced at a depth of about 6 km (Rocchi et al., 2002): the Monte Capanne (7.4–7 Ma, Westerman et al., 2004; Gagnevin et al., 2011) and Porto Azzurro (6.53–6.4 Ma; Gagnevin et al., 2011; Spiess et al., 2021) plutons, and are located on the western and eastern sides of Elba Island, respectively (Fig. 1). Significant circulation of hydrothermal fluids (5.9–5.4 Ma; Lippolt et al., 1995; Maineri et al., 2003; Wu et al., 2019) was associated with the cooling phase of the Porto Azzurro pluton (Fig. 2), which produced skarn and Fe-ore deposits (Dini, 2003; Tanelli et al., 2001; Liotta et al., 2015; Zucchi et al., 2022). Hydrothermal mineralisation was driven by normal and oblique- to strike-slip (transfer) faults, which also played a fundamental role in controlling the emplacement and progressive exhumation of the magmatic body (Dini et al., 2008a; Liotta et al., 2015). Among the normal faults, the Zuccale Fault (Late Miocene-Early Pliocene) represents one of the main regional-scale extensional structures, gently dipping towards the East and contributing to the local unroofing of the Porto Azzurro pluton (Fig. 1b; Keller and Pialli, 1990; Pertusati et al., 1993; Daniel and Jolivet, 1995; Collettini and Holdsworth, 2004; Smith et al., 2011; Spiess et al., 2021). Based on cartographic evidence, the horizontal throw of the Zuccale Fault is estimated to be about 6 km, partially gained after the emplacement of the Porto Azzurro monzogranite (Pertusati et al., 1993). The internal structure of the Zuccale Fault zone, which is up to 5 m thick, has been described in several papers (e.g., Pertusati et al., 1993; Collettini and Barchi, 2004; Collettini and Holdsworth, 2004; Smith et al., 2011; Viola et al., 2022): the shear zone shows S-C and C-C′ structures, clearly indicating a top-to-the-East shear sense (Collettini and Holdsworth, 2004), and the main slip surface is characterised by grooves and mechanical striations with Fe-oxides and/or Fe-hydroxides (Pertusati et al., 1993; Collettini and Barchi, 2004; Liotta et al., 2015). This evidence suggests that the Zuccale Fault evolved from ductile to brittle deformation (Pertusati et al., 1993; Collettini and Holdsworth, 2004; Collettini and Barchi, 2004) when the permeable cataclastic level played the role of conduit and trap for geothermal fluids (Liotta et al., 2015).

3. Methods

Field mapping (Fig. 1c) was carried out in the study area, combined with the collection of structural and kinematic data at 73 structural analysis stations. Geometric parameters of the Fe-hydrothermal veins (i.e., vein length, width, orientation) were collected in key outcrops representative of the entire mineralised study area (see section 6), following the scan area, scan line and scan box methodology to estimate the secondary permeability and efficient porosity (Zucchi et al., 2017).

Eighteen samples of host rocks and veins were collected for petrographic, mineralogical and fluid inclusion analyses (Table S1). Fluid inclusions in quartz crystals, associated with hematite and adularia, were analysed by microthermometry, micro-Raman spectroscopy and SEM-EDS methods to reconstruct the chemical and physical characteristics of the palaeo-fluids. In addition, Sr isotopic analyses were carried out on hematite from two veins and on two host rocks to obtain information on the fluid source(s) and/or fluid-rock interaction processes during the palaeo-fluid flow. Specific information on fluid inclusion and Sr isotopic analytical methods can be found in the Supplementary Material.

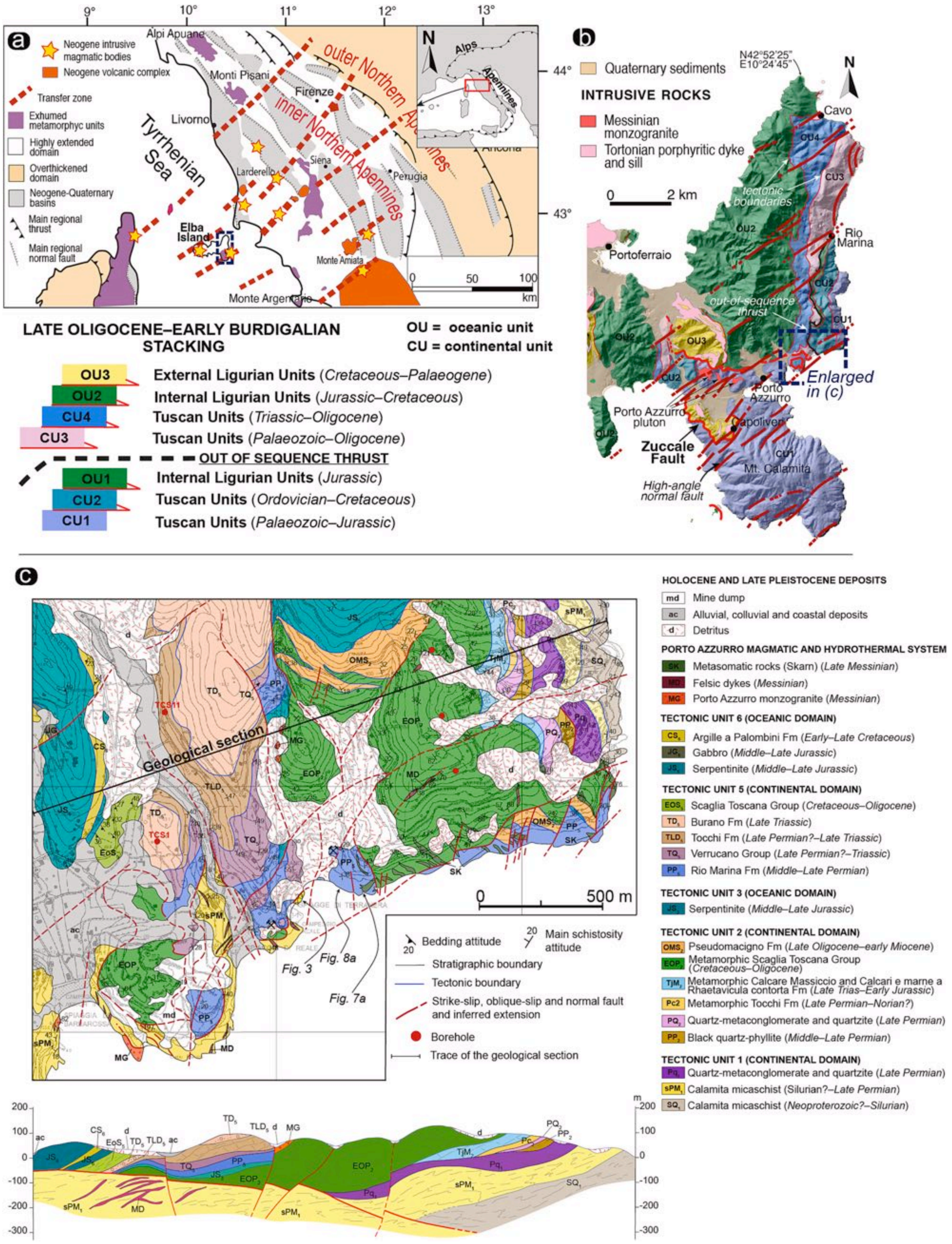

Fig. 1. (a) Structural sketch map of Northern Tyrrhenian Basin and Northern Apennines; (b) geological sketch map of Elba Island and location of the study area (in the black square). The different tectonic units and the main low- and high-angle normal faults are highlighted (modified after Caggianelli et al., 2018); (c) geological map of the study area indicating the Reale and Terranera mining areas and related geological cross section. Its trace is indicated in the map.

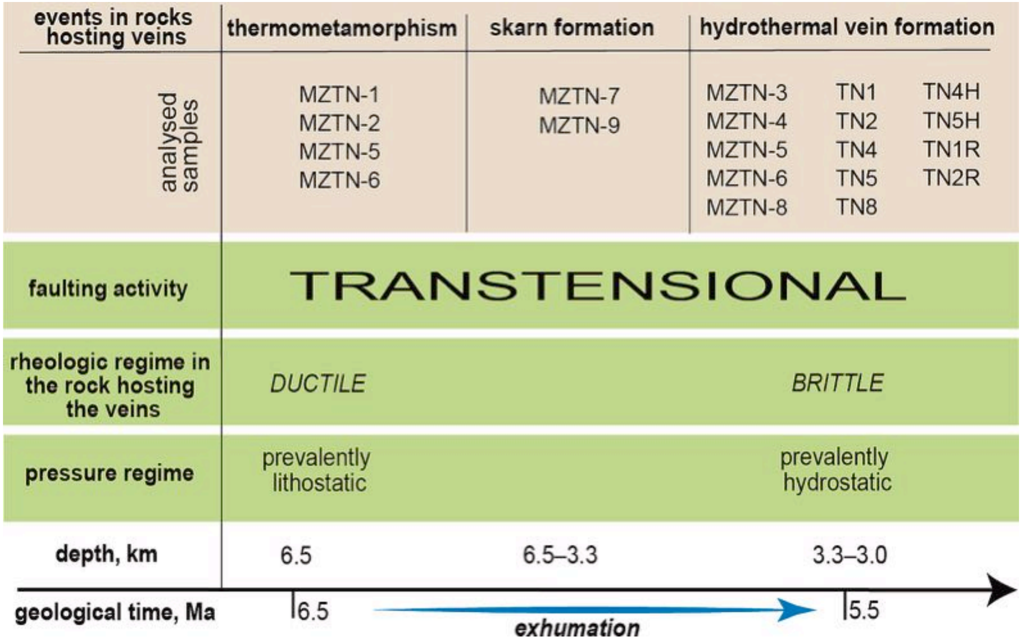

Fig. 2. Time-line diagram illustrating the main geological processes and thermo-rheological conditions active during the time period under study. Names of samples (see also Table S1) are indicated and related to the geological evolution.

4. Geological setting of Reale-Terranera mining area

The Zuccale Fault is well exposed, albeit partially, in the western part of the Reale-Terranera mining area (Duranti et al., 1992; Pertusati et al., 1993; Smith et al., 2011; Musumeci et al., 2015; Garofalo et al., 2023), before dipping slightly to the East and continuing below sea level (Figs. 1c and 3).

The footwall is composed of micaschist intruded by decimetre- to

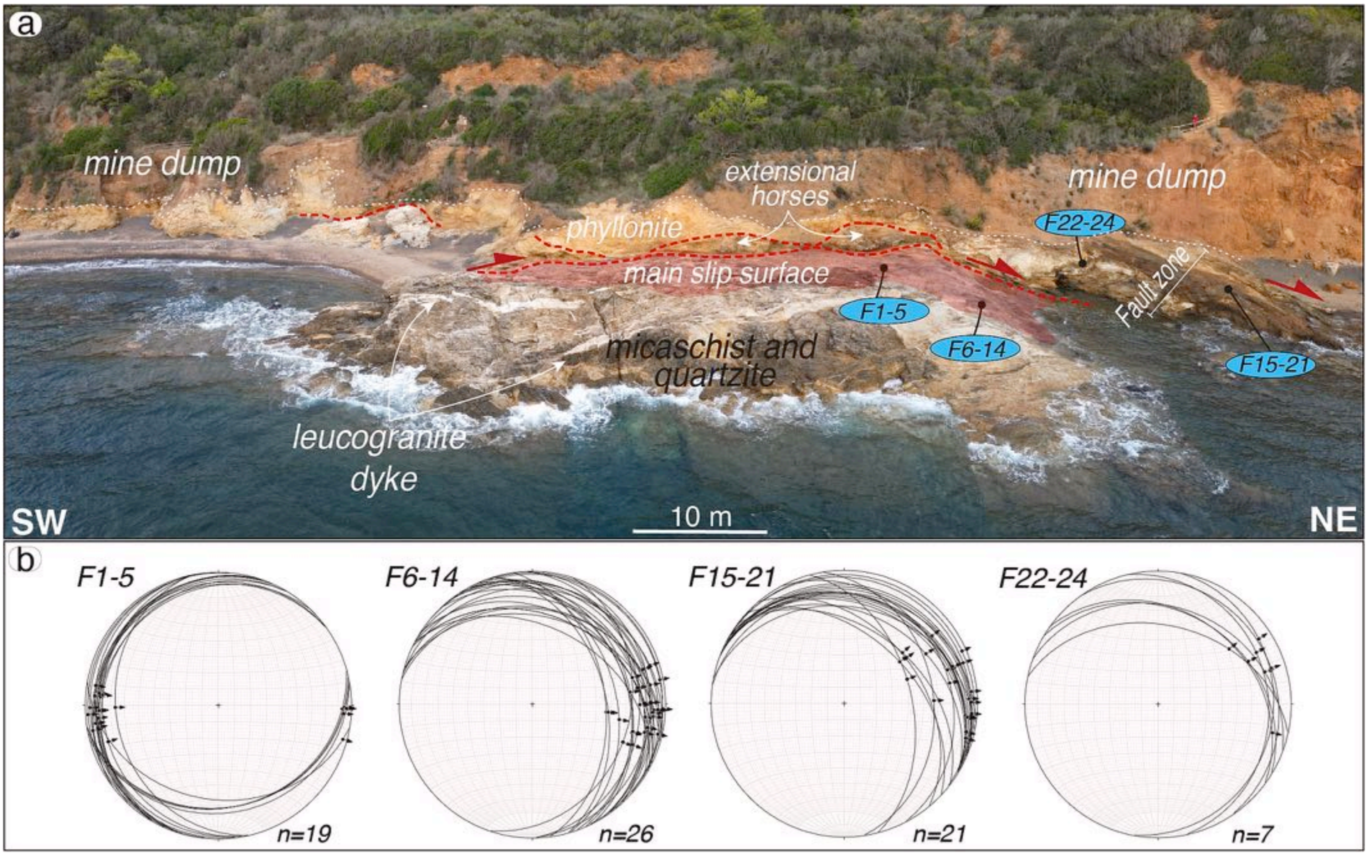

Fig. 3. (a) Panoramic view of the Zuccale Fault exposure in the Terranera area; (b) stereographic diagrams (lower hemisphere, equal-area projection) of structural and kinematic data collected in the footwall of the Zuccale fault (location of the structural stations is indicated in (a)).

metre-thick, tourmaline-bearing leucogranite dykes (Fig. 4), and belonging to the Porto Azzurro Unit (Garfagnoli et al., 2005). The micaschist is also accompanied by foliated quartzite, both characterised by a well-developed schistosity with biotite + andalusite and/or cordierite ± muscovite ± K-feldspar ± plagioclase, thus indicating low-P metamorphic conditions. The occurrence of low-P metamorphism, together with the presence of numerous swarms of leucogranite dykes, suggests proximity to the Porto Azzurro pluton. Indeed, granitic rocks have been drilled at shallow depths during mining exploration (Fig. 5). In particular, close to the coast, one borehole encountered a granitic body hosted in the micaschist, between 45.70 and 51.75 m b.s.l.; another borehole, 800 m to the NW of the study area, drilled a granitoid body from 275 m down to 310.8 m b.s.l. (Montecatini, 1950–1953). These bodies, especially the last one, are reasonably related to the sill swarms that accompanied the Porto Azzurro pluton. The footwall of the Zuccale Fault was also affected by high-angle to low-angle normal faults assisted by tourmaline + quartz syn-kinematic mineralisation (Fig. 4c, d), thus attesting to their activity during magma cooling and subsequent hydrothermal circulation (cf. Viti et al., 2016; Zucchi et al., 2017).

The hanging wall of the Zuccale Fault consists of Triassic siliciclastic units (Verrucano Group) and underlying late Palaeozoic phyllite (Rio Marina Fm). The Verrucano Group is a continental succession composed mainly of white to pink quartz metaconglomerate, grey to green metasandstone, purple to greenish phyllite and metasiltstone. Conversely, the Rio Marina Fm is composed of black to grey marine graphitic phyllite, metasiltstone and metasandstone (Fig. 4e), recently attributed to the middle-late Permian (Guadalupian-Lopingian; Spina et al., 2019). At the thin section scale, the phyllite and metasandstone consist of alternating millimetre to submillimetre domains, rich in quartz and micas (Fig. 4f) with cordierite, as millimetre-sized spots on the main foliation (S_1). The rock fabric is characterised by two overlapping main tectonic foliations (S_1 and S_2), always recognizable at the microscopic scale (Fig. 4f). S_1 is a continuous foliation (sensu Passchier and Trouw, 2005) defined mainly by flattened and elongated quartz grains and homogeneously oriented muscovite and/or biotite (Fig. 4g). S_1 characterises microlithons bounded by the S_2 foliation (spaced schistosity; sensu Passchier and Trouw, 2005),which isolates domains with rough or smooth outlines and is formed by a syn-kinematic mineral assemblage consisting of fine-grained mica, Fe-oxides and quartz (Fig. 4f).

The Zuccale Fault zone, which dips gently to the East, is characterised by discontinuous levels of Triassic limestone and ophiolitic remnants, embedded in a yellowish cataclasite (Figs. 3 and S1), where S-C and C-C′ structures indicate a top-to-the-East shear sense. Kinematic indicators on the fault slip surface (structural stations F1-F24 in Fig. 3) consist mainly of slicken lines and quartz + Fe-oxide and Fe-hydroxides slickenfibres, indicating on average an ESE-oriented tectonic transport (Figs. 3 and S1), in agreement with the data collected at other localities where the Zuccale Fault crops out (Pertusati et al., 1993; Collettini and Barchi, 2004; Collettini and Holdsworth, 2004; Collettini et al., 2006; Smith et al., 2007, 2011; Liotta et al., 2015; Musumeci et al., 2015).

Both the Zuccale footwall and hanging wall are then affected by NNW- to ENE-striking sub-vertical faults with a dominant strike-slip to oblique-slip kinematic component (Figs. 1 and 6) and widespread mineralisation. In the footwall, the faults are locally characterised by ultracataclasite up to 3 cm thick and the mineralisation consists of syn-kinematic tourmaline + quartz, indicating oblique-slip movement with a dominant normal component (Fig. 4c,d). In contrast, in the hanging wall, the mineralisation consists of hematite + magnetite + pyrite + quartz + adularia with widespread metre-scale ore volumes and pockets, mostly developed at the intersection of NNW- to ENE-striking faults. The relationships between fault damage zone fractures and mineralisation were analysed in a few representative outcrops located in the hanging wall of the Zuccale Fault (Fig. 1c).

5. Faults and mineralisation

Samples (Table S1) and data to evaluate the relationships between permeability and fluid flow were collected in the hanging wall of the Zuccale Fault, where outcrop conditions of late Palaeozoic metasandstone and phyllite (Rio Marina Fm) were most favourable. The Rio Marina Fm is locally subjected to metasomatism, laterally passing into a massive skarn ore deposit (Fig. 7a-c) composed of epidote and amphibole (Fig. 7f) with a minor content of quartz and Fe-hydroxides, thus obliterating the original fabric. Epidote has a variable composition ranging from epidote s.s. to clinozoisite, whereas amphibole mostly has a ferro-actinolite or, more rarely, an actinolite composition (Table 1). This ore-deposit is affected by faults and associated Fe-mineralisation, as described below, on the basis of cross-cutting relationships and kinematic data.

5.1. *First fault generation*

It consists of low-angle faults parallel to the Zuccale Fault and NNW- and ENE-striking high-angle faults (Figs. 6a and 8a,b). All of these structures are characterised by the presence of hematite + quartz ± pyrite ± adularia shear and extensional veins, suggesting that they are coeval with the circulation of the same mineralising fluids.

The fault zones of the low-angle normal faults are usually characterised by massive hematite with a minor amount of quartz and occasional pyrite (Fig. 8b). Their minimum displacement exceeds several metres where lithological markers are recognizable. Kinematic indicators on fault slip surfaces consist of syn-kinematic hematite + quartz + adularia slickenfibres, in which hematite is the most abundant mineral phase. The kinematic indicators are often superimposed, suggesting different movements with a dominant eastward tectonic transport (Figs. 6a, 8c and, 9a). Nevertheless, the fault activity continued after the mineralising event (Fig. 8d). Millimetre-thick veins of biotite + quartz + adularia, sub-parallel or at low-angle to these faults, characterise the entire outcrop and probably developed during the early stage of faulting. At the microscopic scale, these veins can be divided into two types on the basis of their mineral composition: i) millimetre-thick veins with biotite crystals often arranged in rosette-shape aggregates and minor amounts of adularia and quartz, occasionally displaying euhedral habit (Fig. 8e); ii) millimetre-thick zoned veins with rosette-shaped aggregates of biotite along the vein margins and quartz + adularia + albite crystals with fine-grained titanium-rich minerals (titanite ± ilmenite) filling micrometre voids, in the central part of the vein (Fig. 8f,g).

The high-angle normal faults (Figs. 6a, 8a,b, and 9) are characterised by cataclasite up to 50 cm thick, cemented by hematite and minor amounts of quartz and pyrite (Fig. 9b). In some cases, mineralised (hematite + quartz) hydraulic breccias characterise the fault zones (Fig. 9c), suggesting that the hydrothermal fluid pressure locally exceeded the confining pressure during faulting. Kinematic indicators on the slip surfaces consist of hematite slickenfibres and subsequent slickensides (Fig. 9a). Occasionally superpimposed movements can be recognized indicating a first movement with a dominant right-lateral slip, followed by a second movement with a dominant normal component.

Along the fault planes, centimetre- to decimetre-thick extensional jogs were formed with hematite + quartz ± pyrite ± adularia (Fig. 9d, e). When present, adularia crystals usually occur in the central part of the syntaxial vein, being the last mineral phase to form (Fig. 9e). Tensional veins of hematite + quartz ± pyrite ± adularia, up to 5 cm thick, developed at low- to middle-angle to the fault surface, and their angular relationships are consistent with right-lateral movement, according to kinematic indicators on the slip surfaces. These veins are often characterised by a zoned mineralisation, defined by hematite + quartz ± pyrite and quartz, in the central and peripheral zones, respectively (Fig. 9f).

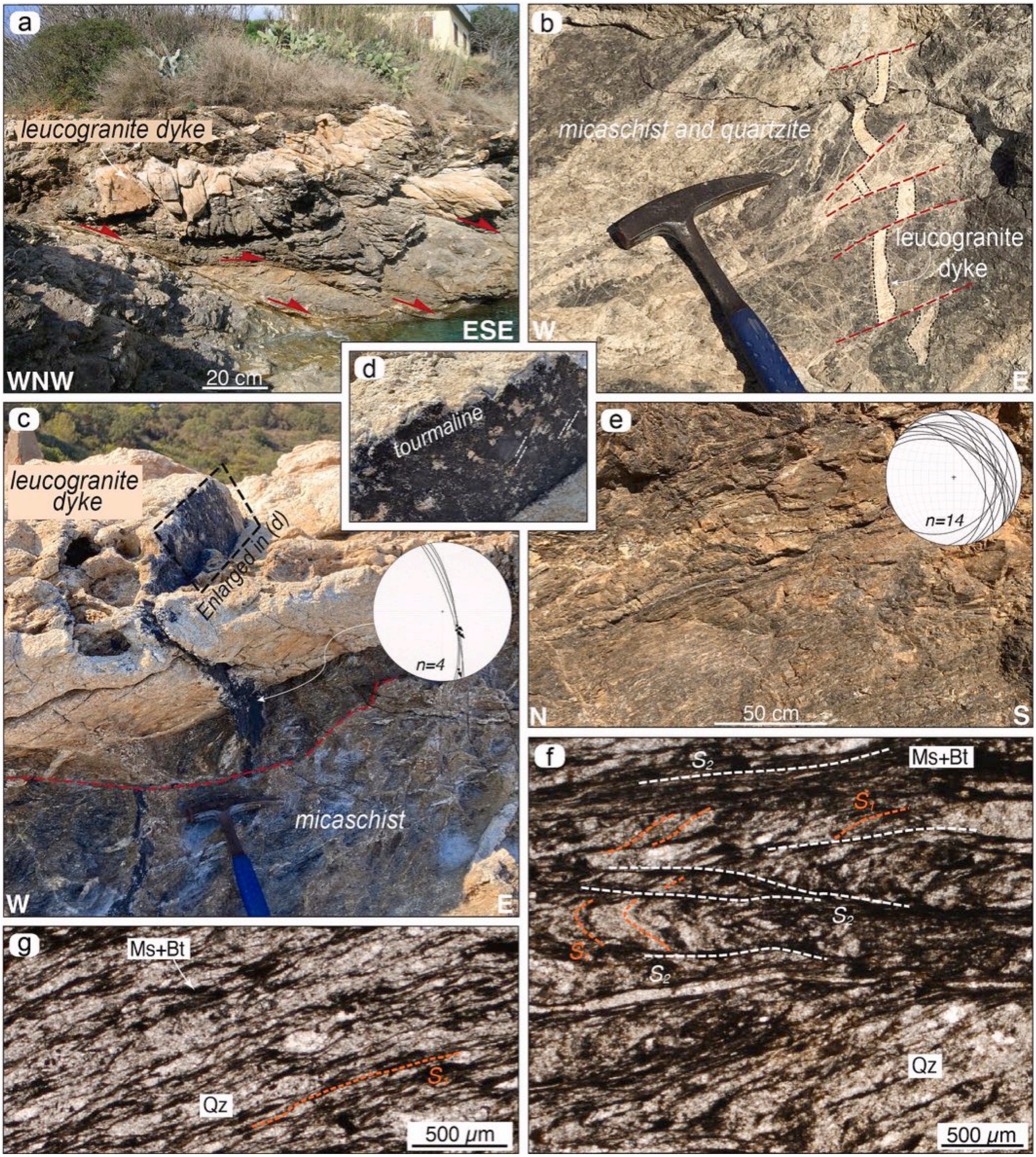

Fig. 4. (a) Micaschist belonging to the Mt. Calamita Fm, cropping out in the footwall of the Zuccale fault, and intruded by tourmaline-rich leucogranite dykes. Micaschist and dykes were both crosscut by low- and high-angle normal faults; (b) detail of leucogranite dyke dissected by low-angle normal faults; (c) high-angle normal fault crosscutting a tourmaline-rich leucogranite dykes characterised by tourmaline + quartz slickenfibres on the slip surface showing two different movements (detail in d); (e) metasandstone, phyllite and quartzite belonging to the Rio Marina Fm cropping out in the hanging wall of the detachment; (f) micrograph (plane polarised light) of metasandstone and quartzitic phyllite showing a compositional layering defined by quartz-rich and phyllosilicate-rich levels, in which two superposed tectonic foliations (S_1 and S_2) can be recognized; (g) micrograph (plane polarised light) showing elongated quartz crystals and platy phyllosilicates (muscovite + biotite) with a preferred orientation.

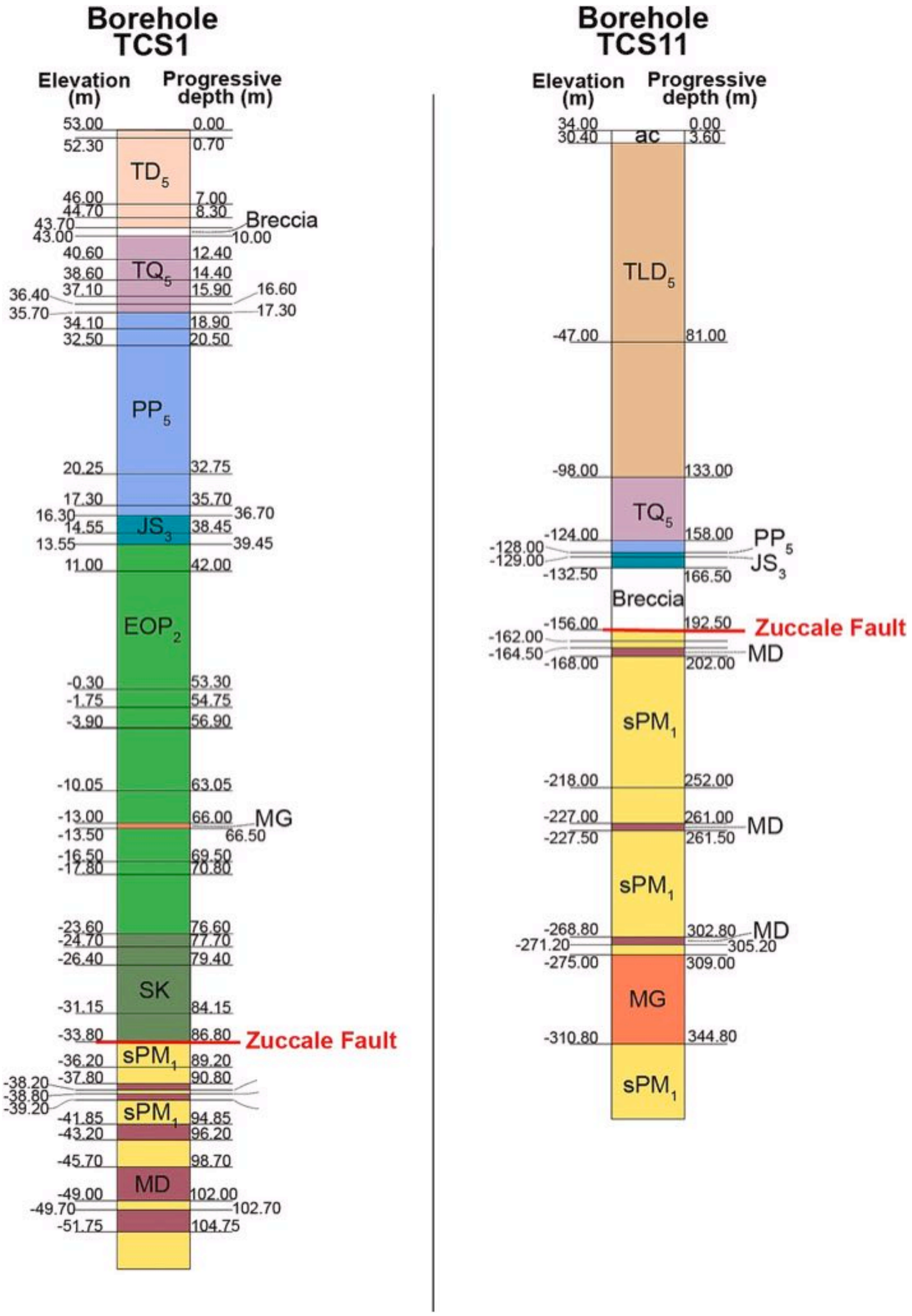

Fig. 5. Boreholes stratigraphic logs drilled nearby the study area (see Fig. 1c for their location). Symbols as in Fig. 1c.

Both low- and high-angle faults dissect the magnesian Fe-skarn (Garofalo et al., 2023). The veins associated with these faults are characterised by centimetre-scale lateral branching, determined by fluid flow into pre-existing foliations (Fig. 7d). In some places, sub-millimetre amphibole aggregates are concentrated near the intersection with the hematite + quartz ± pyrite veins and often penetrate quartz crystals (Fig. 7e,g).

5.2. *Second fault generation*

The second generation of faults is exposed in only a few zones, mostly on the eastern side of the study outcrops (Fig. 8b). It consists of NE-striking high-angle faults characterised by cataclasite up to a few centimetres thick and the absence of mineralisation (Figs. 6b and 9g-i). Where present, kinematic indicators consist of slickensides, chatter marks, lunate structures and intersections between fractures and fault planes indicating right-lateral oblique-slip movements (Figs. 6b and 9i) in the same tectonic context.

6. Secondary permeability estimation

Secondary permeability estimates of the fault zones were calculated considering the geometric parameters collected in the field, following the methodology described in Zucchi et al. (2017). In a representative area, a detailed structural map at 1:100 scale (scan area) was first realised to reconstruct the alignments of the mineralised fault zones (Figs. 7a, 8a and S2). Three scan lines (up to 16.5 m long and 3 m apart), were located within the scan area. Their orientation is roughly E-W trending, to be orthogonal to the NNW-striking structures with the aim of measuring vein spacing.

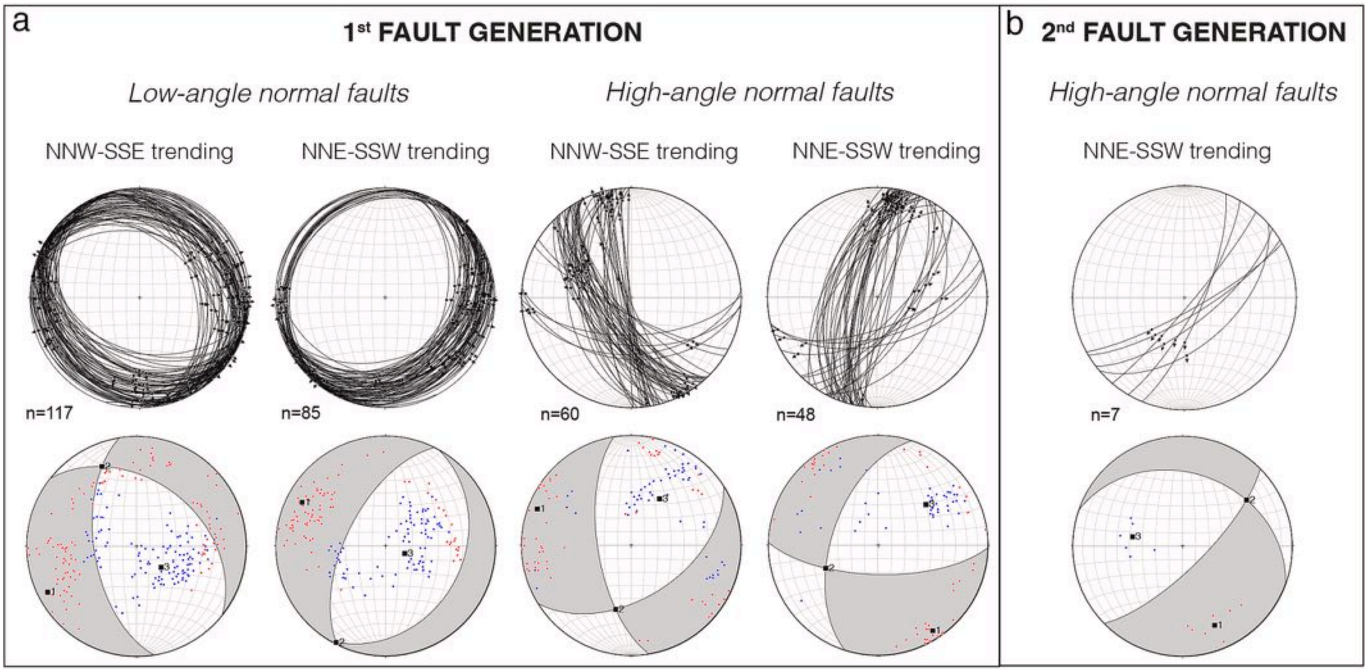

Fig. 6. Cumulative stereographic diagrams (lower hemisphere, equal-area projection) of low- and high-angle normal faults kinematic data, divided in the first (a) and second (b) generations. Red and blue dots indicate pressure (P) and tension (T) axes, respectively. Black squares show the orientation of the stress axes, as labelled. (For interpretation of the references to colour in this figure legend, the reader is referred to the web version of this article.)

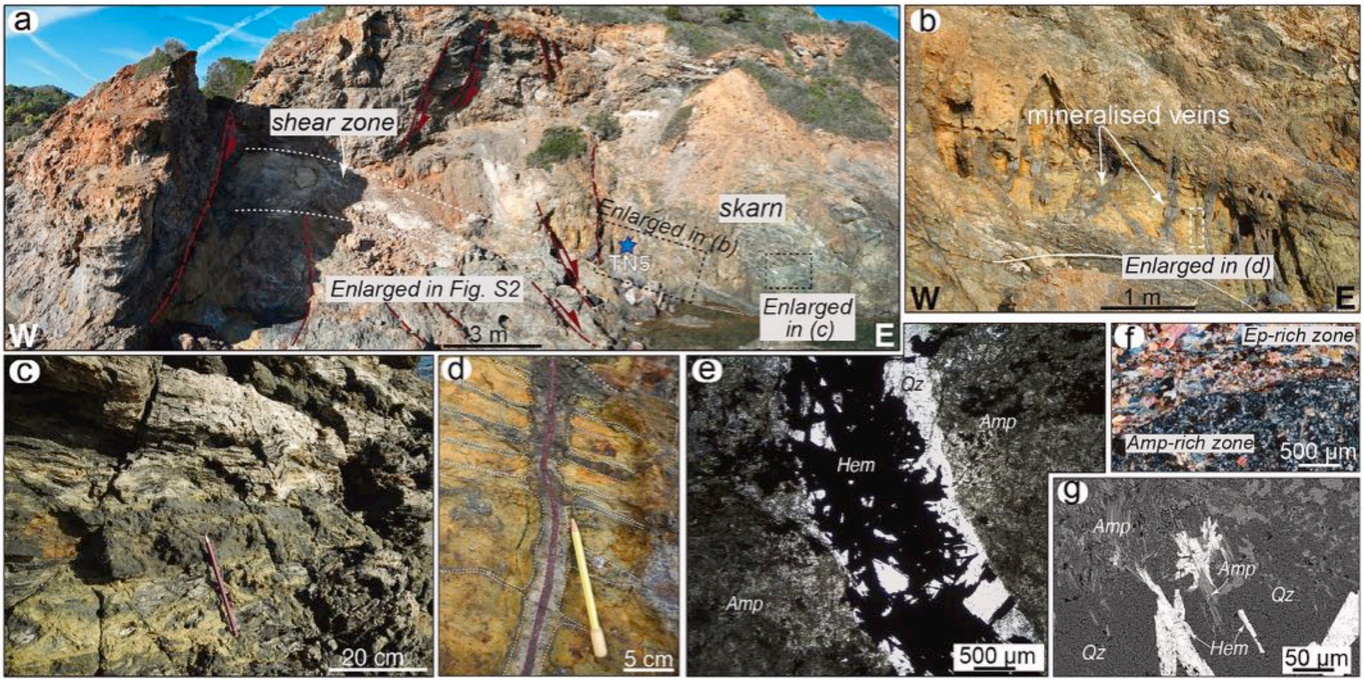

Fig. 7. (a) Panoramic view of the detailed study area (see also Fig. 8a) where skarn deposit is shown; the location of sample TN5 for fluid inclusions is shown; (b) panoramic view of part of the skarn wall, crossed by hematite + quartz ± pyrite veins up two metres long; (c) detail of the skarn body; (d) detail of a vein crossing the skarn shown in (b) and where thinner mineralised branch veins pervaded laterally the wall rock; (e) micrograph (plane polarised light) of hematite + quartz veins crossing the skarn; (f) micrograph (cross polarised light) of skarn mainly made up of epidote- and amphibole-rich zones separated by a thin vein formed by hematite and minor amount of Fe-hydroxides; (g) SEM-BSE image showing a detail of a vein edge in which amphibole penetrates quartz crystals. Mineral abbreviations according to Whitney and Evans (2010).

The minimum and maximum widths and lengths of each mineralised vein were then recorded within each 40×40 cm scan box, shifted 1 m laterally along the scan lines. The size of the scan boxes was determined by the minimum distance between two adjacent similar fault-slip zones, resulting in 0.4 m per side. The scan box spacing along the scan line was set at 1 m considering the smallest value of the maximum shear vein spacing value (i.e., 1.2 m). The collection of the geometric parameters within each scan box was carried out in the field where the size of the

Table 1

Representative SEM-EDS analyses of amphibole, epidote and biotite from skarn deposit and biotite from vein.

wt%	MZTN8 Anf-06	MZTN8 Anf-02	MZTN8 Anf-01	MZTN8 Ep-05	MZTN8 Bt-02	MZTN2 Bt-Hem-03
	Ferro-actinolite	Ferro-actinolite	Actinolite	Epidote	Biotite	Biotite
SiO_2	48.31	49.77	53.36	37.71	41.54	36.63
TiO_2				0.22	0.27	
Al_2O_3	1.88	2.19	0.92	24.56	12.42	15.75
FeOt	28.56	28.04	15.82	9.63	17.31	24.47
MnO	0.52	0.38	0.49		0.27	0.46
MgO	3.86	4.10	13.06		13.16	8.89
CaO	11.44	11.31	12.16	23.92	0.59	0.20
Na_2O	0.37	0.33	0.25		0.24	0.14
K_2O	0.26	0.22	0.18		8.57	6.50
tot	95.20	96.34	96.24	96.04	94.37	93.04
O eq.*	23	23	23	25	22	22
Si	7.78	7.85	7.93	6.01	6.26	5.77
Al^{IV}	0.22	0.15	0.07		1.74	2.23
Al^{VI}	0.14	0.25	0.09	4.61	0.46	0.69
Ti				0.03	0.03	
Fe^{3+}				1.28		
Fe^{2+}	3.85	3.70	1.96		2.18	3.22
Mn	0.07	0.05	0.06		0.03	0.06
Mg	0.93	0.96	2.89		2.95	2.09
Ca	1.97	1.91	1.94	4.08	0.09	0.03
Na	0.12	0.10	0.07		0.07	0.04
K	0.05	0.04	0.03		1.65	1.31
∑cat	15.13	15.01	15.04	16.01	15.46	15.44
XMg	0.19	0.21	0.60		0.58	0.39
$X_{Fe3+} = Fe^{3+}/(Fe^{3+}+Al)$				0.22		

eq* = oxygen equivalent.

mineralised structures was suitable for direct measurement. Conversely, for structures smaller than one millimetre, measurements were made by image analysis (using ImageJ 1.45 software) using pictures taken at right angle to the scan box surface. The dataset consists of 540 data and is summarized in Fig. S2, where the diagrams illustrate: i) the frequency and fracture density; ii) the average of the minimum and maximum aperture of each structure; iii) the secondary permeability; iv) the efficient porosity.

Finally, the secondary permeability was calculated using the equation proposed in Zucchi et al. (2017). Thus, the low-angle normal faults show secondary permeability values in the order of 10^{-15} m^2, while the high-angle normal faults show values up to 10^{-13} m^2.

7. Fluid inclusions

Fluid inclusions were analysed in quartz crystals from five samples (TN1, TN2, TN4, TN5 and TN8) of quartz-hematite veins collected in the study area (Fig. 8a and Table S1). Specifically: TN1, TN4 and TN5 are representative of shear veins (e.g., Figs. 7d and S2a) with sizes up to 5–6 cm, whereas TN2 and TN8 are from extensional jogs (e.g., Figs. 9d and S2a). Samples from shear veins consist of quartz crystals, often with euhedral habitus, surrounded by a dominant hematite matrix, which in some cases penetrates the quartz. Unlike the other samples, sample TN5 was collected from a hematite + quartz vein that crosscut the skarn deposit (Fig. 7d). At the microscope scale, the veins show mostly hematite + quartz mineralisation with amphibole crystals embedded in quartz (Fig. 7e,g).

7.1. Fluid inclusion petrography

Optical microscope observations reveal that most fluid inclusions occur along trails (Fig. 10a,b), while other inclusions are clusters arranged in a three-dimensional random distribution, suggesting their primary origin (Roedder, 1984; Shepherd et al., 1985; Goldstein, 2003) (Fig. 10c,d). In most cases, the secondary or pseudo-secondary nature of the fluid inclusions along the trails cannot be ascertained. However, a few late trails clearly crosscut the edge of the quartz grains and are therefore considered secondary (Fig. 10a). No evident alignments of fluid inclusions along the morphological features of the host quartz were observed.

At room temperature, most fluid inclusions are two-phase (liquid+vapour), defined by liquid-rich inclusions with an apparently homogenous liquid-to-vapour ratio, as the liquid phase represents 75–80% of the total inclusion volume. However, fluid inclusions with a variable liquid-to-vapour ratio, as well as rare one single-phase (liquid-only) inclusions associated with two-phase inclusions, were also observed in a few trails and clusters (Fig. 10e). These occurrences suggest that necking-down processes have affected such fluid inclusion assemblages (Shepherd et al., 1985; Goldstein, 2003). Some inclusions contain one or more accidentally trapped colourless or green solids (Fig. 10f,g). An accidentally trapped red solid (probably hematite) was also observed in one case.

Most of the observed fluid inclusions have a size ranging from 2 to 20 μm; a maximum size of 90 μm is only sporadically observed. Fluid inclusions are characterised by dominantly irregular shapes, even though almost regular (rounded to ovoidal) forms are also observed, especially for those inclusions aligned along trails.

7.2. Microthermometric analyses

Fluid inclusion assemblages (FIAs, as defined by Goldstein and Reynolds, 1994) consisting of 3 to 16 fluid inclusions were selected for microthermometry. In order to consider data from fluid inclusions that are truly representative of an original homogenous trapped fluid, we have selected only those FIAs showing relatively consistent homogenisation temperatures (T_h) values falling within a 15 °C interval, following Goldstein and Reynolds (1994).

A total number of 221 fluid inclusions were analysed. The microthermometric results of fluid inclusions along trails and in clusters from the 5 examined samples, are reported in Table S2 and summarized in

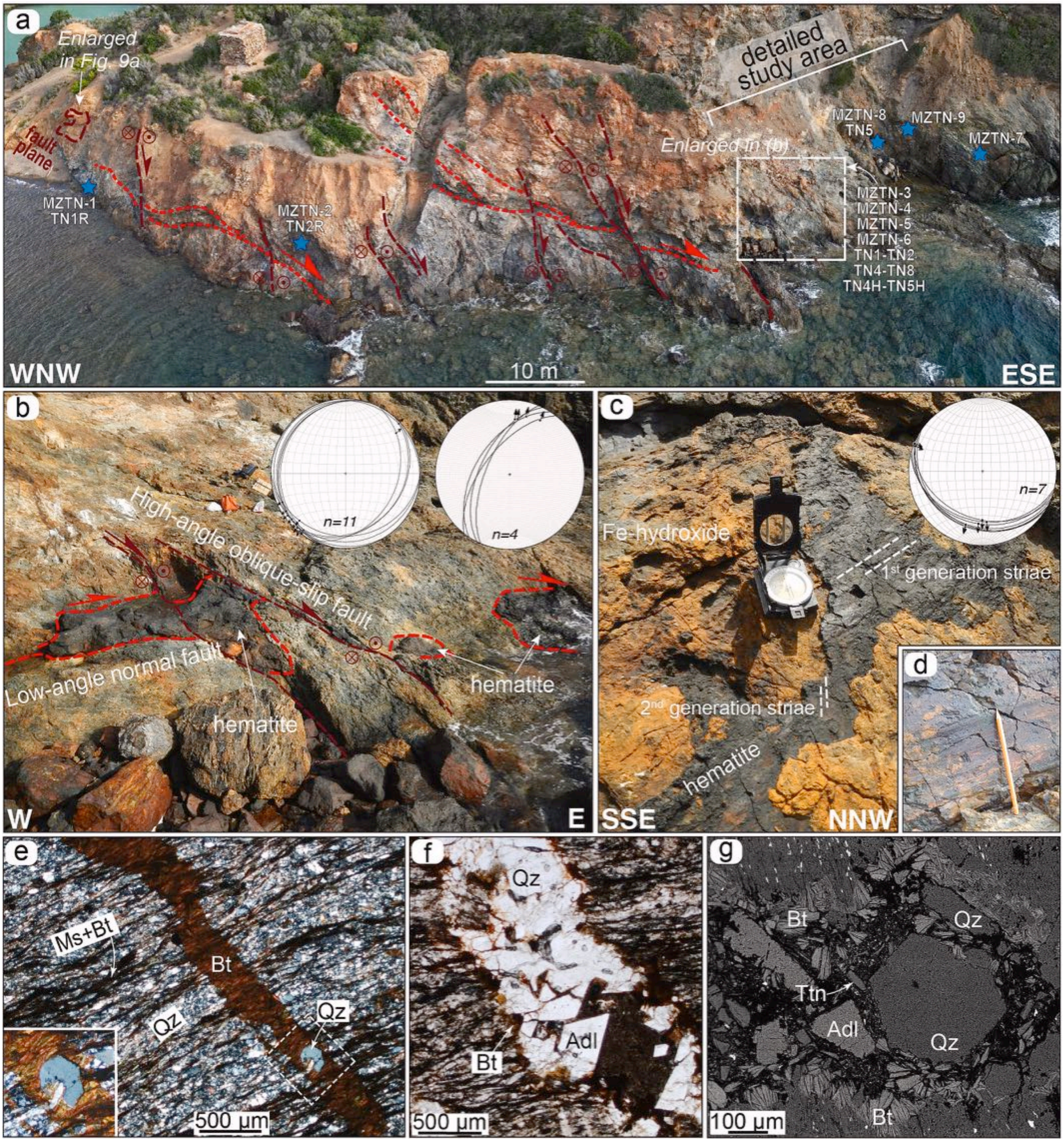

Fig. 8. (a) Panoramic view of the Terranera wall in which the main low- and high-angle normal faults of first generation and their crosscutting relationships are highlighted. Location of samples (blue stars) is shown. Structural and kinematic data of Fig. 6 were mainly collected along this exposure; (b) detail of low- and high-angle faults crosscutting relationships; (c) detail of low-angle fault slip surface characterised by hematite ± quartz slickenfibres showing two superposed movements; (d) mechanical striation on the slip surface; (e) micrograph of millimetre-thick first type of veins related to the low-angle normal fault and orthogonally cutting the main foliation of the rock (cross polarised light). In the inset a detail of euhedral quartz embedded within biotite; (f) example of the second vein type mainly filled by quartz and adularia with biotite crystals occurring along the vein edges (plane polarised light); (g) SEM-BSE image of the second vein type characterised by hexagonal section of quartz and adularia crystals surrounded by biotite showing the typical rosette-shape within a fine-grained matrix mainly made up of titanite and ilmenite (cross polarised light). Mineral abbreviations according to Whitney and Evans (2010). (For interpretation of the references to colour in this figure legend, the reader is referred to the web version of this article.)

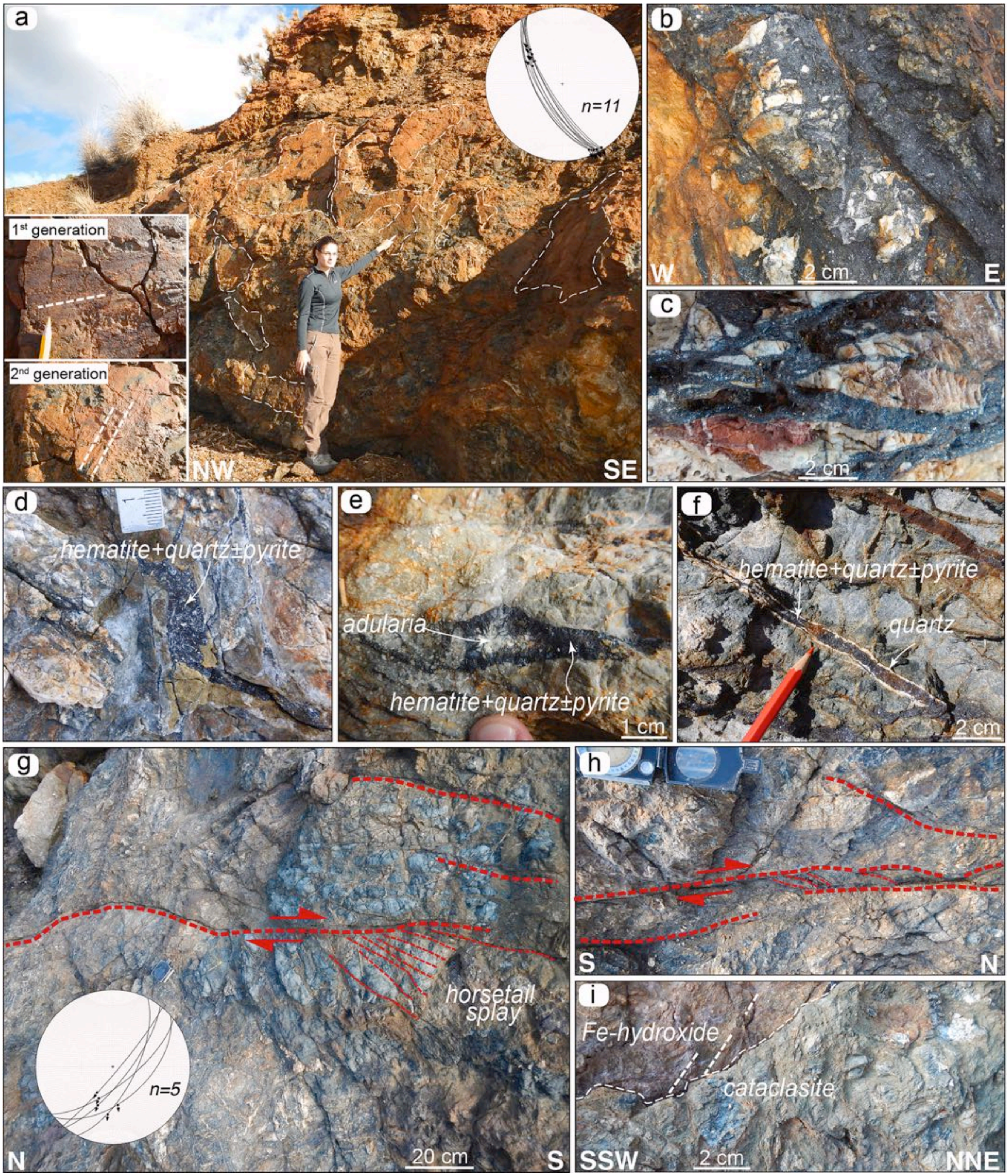

Fig. 9. Examples of high-angle normal faults. (a) NNW-SSE trending fault plane of the first generation with two different hematite + quartz slickenfibres; (b,c) details of cataclasite, mostly cemented by hematite and hydraulic breccia; (d) example of an extensional jog mainly filled by hematite + quartz ± pyrite, and (e) adularia + hematite + quartz ± pyrite. Adularia developed mostly in the central part of the jog whereas hematite + quartz ± pyrite are concentrated along the edges; (f) example of zoned vein made up of hematite ± pyrite in the central part and mostly quartz at the contact with the host rocks; (g) NE-SW trending fault with right-lateral oblique slip movements belonging to the second generation and exposed in limited outcrops; (h) detail of a fault zone devoid of syn-kinematic mineralisation; (i) detail of cataclastic level locally characterised by mechanical striations and Fe-hydroxides.

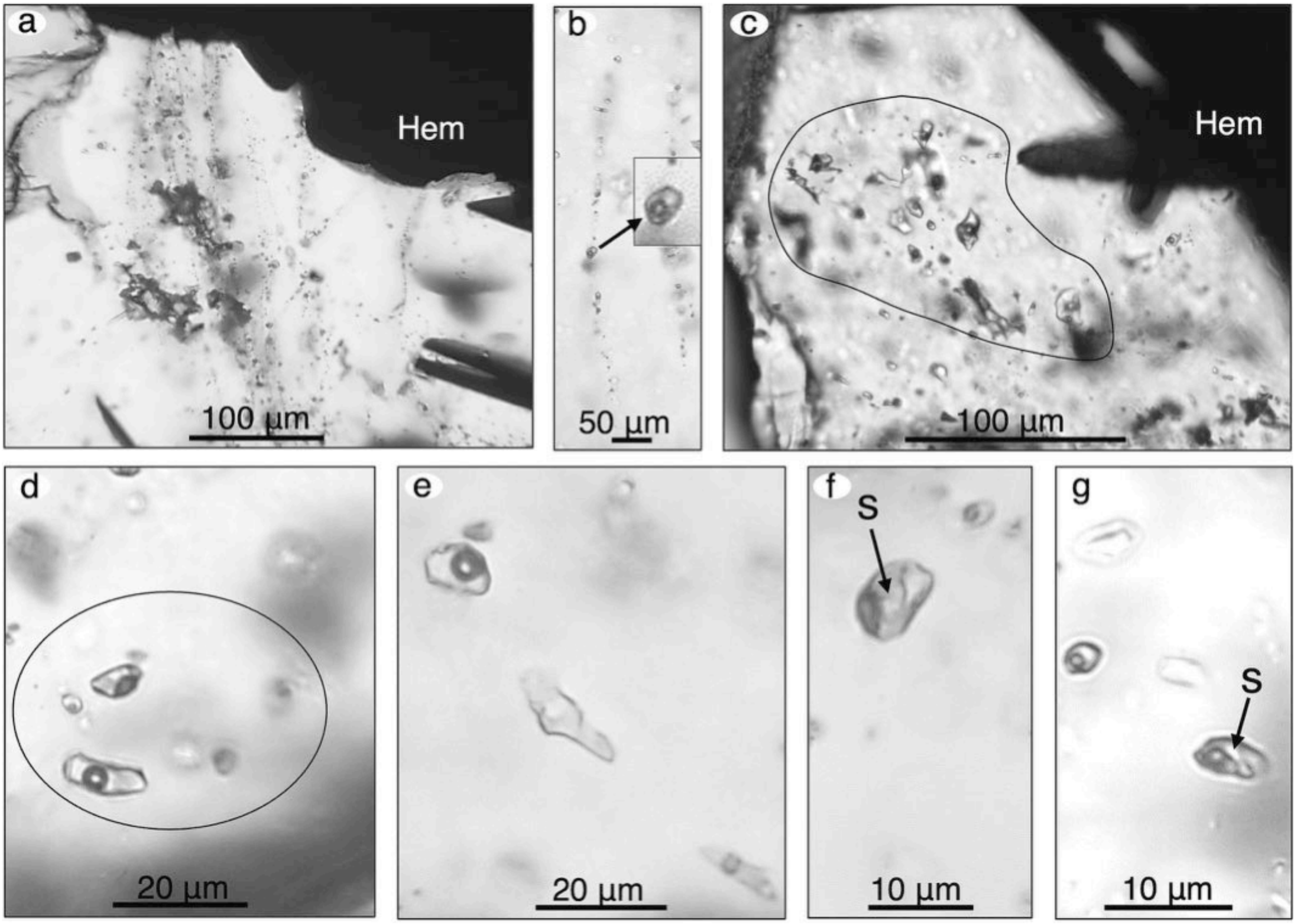

Fig. 10. Micrographs (plane polarised light) of fluid inclusions in quartz. (a) Fluid inclusion trails crosscutting the crystal edge; the opaque phase at the contact with the quartz crystal is hematite (Hem); (b) fluid inclusion trail totally included in the quartz crystal, the row indicates an enlargement of one fluid inclusion; (c,d) fluid inclusion clusters; (e) one-phase (only liquid) fluid inclusion coexisting with two-phases (liquid+vapour) fluid inclusions one of which (top left) characterised by a relatively large bubble; (f,g) fluid inclusions characterised by the occurrence of accidentally trapped solid(s).

Table 2

Summary of the microthermometric data and salinity for fluid inclusions analysed at Terranera. Salinity was computed by the equation of Bodnar (1993) for the H_2O-NaCl system also for inclusions in which ice melted at temperature below the eutectic temperature (-21.1 °C) of the H_2O-NaCl system by extrapolating this equation below such temperature. Abbreviations: T_{mhh} = final hydrohalite melting temperature; T_{mi} = final ice melting temperature; T_h = homogenisation temperature; n. of meas. = number of measurements; n.m. = not measured.

Sample	Occurrence	T_{mhh} (°C)	n. of meas.	T_{mi} (°C)	n. of meas.	T_h (°C)	n. of meas.	Salinity (wt% NaCl eq.)
TN1	clusters	n.m.	–	n.m.	–	311.0/318.1	4	–
TN1	trails	n.m.	–	-23.3/-21.5	7	309.5/319.6	8	23.4/24.5
TN2	clusters	n.m.	–	-25.0/-24.5	3	296.4/306.4	9	25.3/25.6
TN2	trails	-26.7/-28.4	2	-26.7/-15.7	11	287.4/348.8	36	19.2/26.6
TN4	clusters	-21.8/-22.9	2	-26.4/-24.5	7	316.7/347.0	21	25.3/26.5
TN4	trails	n.m.	–	-23.7/-19.1	13	293.7/337.2	31	21.7/24.8
TN5	clusters	-26.8	1	-26.4/-25.6	4	323.8/347.8	11	26.0/26.5
TN5	trails	n.m.	–	-26.1	1	341.5/350.1	3	26.3
TN8	clusters	-20.1/-25.3	5	-24.3/-19.7	25	285.7/346.8	35	22.1/25.2
TN8	trails	-23.3/-26.8	8	-26.6/-14.2	33	293.2/354.8	61	18.0/26.6

Table 2 and Fig. S3. Homogenisation always occurs into the liquid phase by disappearance of the vapour bubble; the overall T_h range is from 285.7 to 354.8 °C (Table 2). The lowest T_h values (<300 °C) are found in samples TN8, TN2 in both clusters and trails, and in sample TN4 in trails. The highest T_h values (>350 °C) are shown by the inclusions in TN5 and TN8 only in trails (Table 2). In general, the whole T_h ranges of fluid inclusions in clusters and trails are similar (Fig. S3a,b).

When the fluid inclusions were cooled during low-temperature experiments, the liquid phase changed into a microcrystalline mass between about -65 and -70 °C. Successive heating resulted in the coarsening of microcrystals at about -60 °C. The apparent first melting temperature (T_{fm}), between about -51 and -45 °C, is indicated by the appearance of rounded and relatively large crystals in the biggest inclusions (i.e., >15 μm). In other inclusions, usually those of small size (i.e., <10 μm), the clear presence of a liquid phase was observed at temperatures >-40 °C. After the first melting, only one solid (ice) was observed in most of the inclusions, possibly due to metastability processes that can inhibit solid(s) nucleation in inclusions (Baumgartner and Bakker, 2009), or because of the optical resolution of the microscope which does not allow the observation of other solids (i.e., hydrohalite and/or other hydrates) in the smaller inclusions. The final ice melting temperature (T_{mi}) in the examined inclusions ranges from -26.7 to -14.2 °C (Table 2 and Table S2), with inclusions aligned along trails showing the highest T_{mi} values (Fig. S3c,d).

In some relatively large inclusions (usually with length >15–20 μm), two distinct solid phases (ice and hydrohalite) can be distinguished after the first melting temperature; repeated temperature heating-cooling cycles (Haynes, 1985), allowed to nucleate two separate single crystals, one of ice and one of hydrohalite (Fig. 11). In four of these inclusions, the last solid to melt was hydrohalite, as T_{mi} was observed between -26.3 and -24.2 °C, while the hydrohalite melting temperature (T_{mhh}) occurred between -23.8 and -20.1 °C (Table 3). In all other inclusions, the melting sequence is opposite, with T_{mhh} values between -28.4 and -23.3 °C and T_{mi} values ranging from -25.6 to -15.7 °C (Table 3). In addition, some inclusions showed, at temperature above T_{mi} and/or T_{mhh}, the presence of a small solid phase, nearly indiscernible from the liquid, usually at the contact between the liquid and the gas bubble. The latter exhibited Brownian motion during heating until the solid phase disappeared. These features, together with the detection of CO_2 in the vapour bubble by micro-Raman analyses (see section below), suggest that such phase might be clathrate. This phase apparently melted between -17.8 and -13.4 °C (Table S2). In all other inclusions, temperature cycling did not evidence the presence of clathrate after ice and/or hydrohalite melting.

7.3. *Micro-Raman analyses*

Micro-Raman spectroscopy was applied to better understand the composition of the fluid system and to identify the solids present in some fluid inclusions. For selected inclusions of TN4 and TN8 samples, spot analyses were performed on both the liquid phase and the vapour bubble. Analyses on inclusions that displayed clathrate melting, showed the presence of CO_2 in the bubble, while the other volatile phases (i.e., CH_4, N_2 etc.) were not detected. Furthermore, CO_2 is also present in the bubble of inclusions where no clathrate was observed by microthermometry (Fig. S4a).

The analysis on the liquid phase always showed a small but sharp peak at about 8[illegible]0 cm^{-1} (Fig. S4b), corresponding to the strongest peak of dissolved $B(OH)_3$ (Frezzotti et al., 2012). Some solids accidentally entrapped within the fluid inclusions are characterised by a small peak at about 1084 to 1087 cm^{-1}, suggesting that these solids are carbonates. One green solid entrapped within sample TN8 showed peaks at 669, 759, 3679 cm^{-1}, probably corresponding to strong peaks of biotite or clinochlore (Frezzotti et al., 2012). Finally, Raman analysis confirmed that the red solid observed in one inclusion is hematite.

7.4. *SEM-EDS analyses*

Fluid inclusions thermal decrepitation was carried out on some remaining quartz fragments of TN4 and TN8 wafers. The salt residues (evaporates) resulting from this procedure, deposited on the wafer surface, usually consist of aggregates of globular solids with irregular or rounded shapes and sizes of about 1–10 μm (Fig. 12a,b). Spot SEM-EDS analyses on different points reveal an inhomogeneous composition of the aggregates. Thus, the analyses were carried out by scanning the whole visible surface of the aggregates (Fig. 12a,b). The boxplot diagram in Fig. 12c summarises the semi-quantitative concentration of the elements (Na, K, Ca, Fe, Mn, Mg, Cl and S) detected by SEM-EDS analyses, while the complete set of analyses is reported in Table S3.

Although this method provides only semi-quantitative estimations of salt composition (Haynes et al., 1988), our results clearly indicate that the most abundant cation (in terms of atoms %) in the evaporates is Na (between 51.2 and 27.7 atoms %), and that, in general, moderate amounts of Ca and K (mostly in the ranges 17.3–3.4 and 10.1–0.3 atoms %, respectively) and minor concentrations of Fe, Mn and Mg (≤2.5, ≤1.4 and ≤1.5 atoms %, respectively) are also present (Fig. 12c, Table S3). Only in one case the Ca content (23.3 atoms %) is slightly lower than the Na content (27.7 atoms %) (Table S3). Chlorine concentrations are from 40 to 49 atoms %; in addition, small amounts of S (≤2.5 atoms %), presumably in the form of SO_4 anion, were found in almost all aggregates (Fig. 12c, Table S3).

All analyses are electrically unbalanced because of anion deficiency in the salt residues. For example, the difference between the positive and negative charges in the analyses reported in Fig. 12a,b is 20.7 and 22.4 for the TN4 and TN8 salt residues, respectively. The charge unbalance could be at least in part related to the presence of borates in the evaporates (boron cannot be detected by SEM-EDS). Indeed, as indicated by micro-Raman analyses, dissolved $B(OH)_3$ occurs in the liquid phase of inclusions. The reactions of $B(OH)_3$ with the cations present in the liquid during thermal decrepitation, can produce the cation-bearing borates and HCl, the latter lost by volatilization. Moreover, considering the presence of CO_2 (detected by micro-Raman analyses) in the gas bubble,

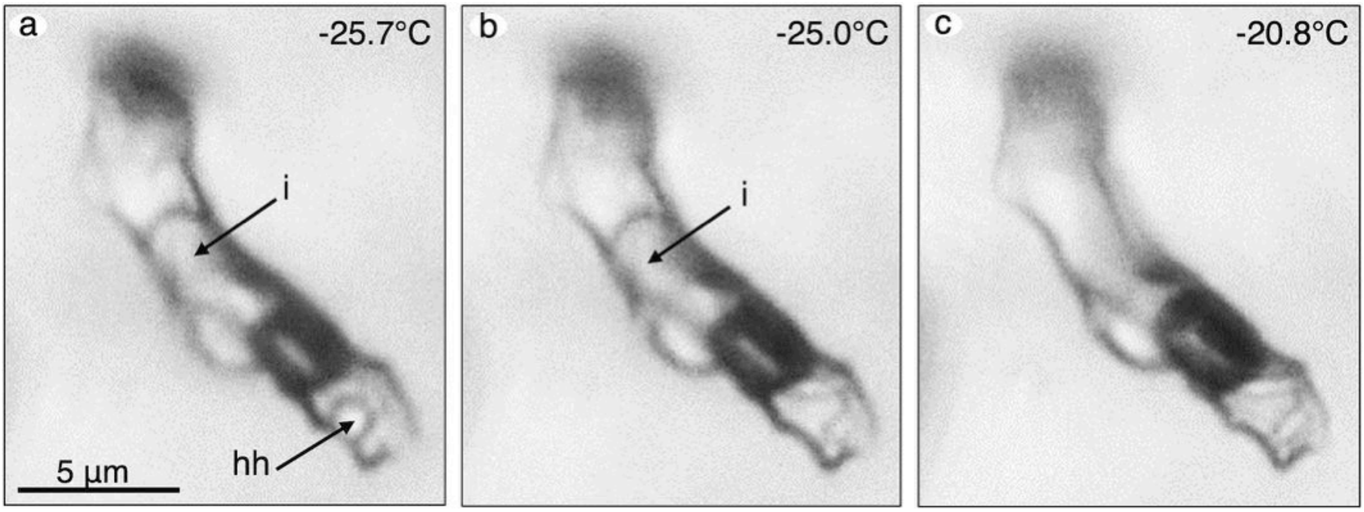

Fig. 11. Micrographs (plane polarised light) of a fluid inclusion during heating and after temperature cycling at low temperature which allowed to nucleate single crystals of ice (i) and hydrohalite (hh); (a) both hydrohalite and ice are present at -25.7 °C; (b) only ice is present at -25 °C just after hydrohalite melting; (c) at -20.8 °C just after final ice melting.

Table 3

NaClˆ, $CaCl_2$ˆ, NaCl+$CaCl_2$ˆ concentrations in weight % (wt%) and NaCl/(NaCl+$CaCl_2$) molar ratio (R_{mol} microth.) for fluid inclusions showing both final ice (T_{mi}) and hydrohalite (T_{mhh}) melting temperatures computed by using the spreadsheet of Steele-MacInnis et al. (2010). NaCl* concentration (total salinity), computed from T_{mi} by using the equation of Bodnar (1993), and NaCl/(NaCl+$CaCl_2$) molar ratio mean and range, computed from SEM-EDS analyses of salt residues (R_{mol} SEM-EDS), are also shown for comparison.

Sample/ fragment	Inclusion's number	Occurrence	T_{mi} (°C)	T_{mhh} (°C)	NaClˆ (wt %)	$CaCl_2$ˆ (wt %)	NaCl + $CaCl_2$ˆ (wt%)	NaCl* (wt% eq.)	R_{mol} microth.	R_{mol} SEM-EDS
TN8/I_X1/1	8	trail	-24.2	-23.8	15.8	8.6	24.4	25.1	0.78	
TN8/I_X/3	16	cluster	-19.8	-25.2	12.0	9.4	21.4	22.2	0.71	
TN8/I_X/5	25	trail	-21.0	-25.0	12.8	9.4	22.2	23.0	0.72	
TN8/I_X/5	27	trail	-20.5	-23.3	16.3	5.9	22.2	22.7	0.84	
TN8/I_X/9	46	trail	-16.3	-23.8	13.2	6.1	19.2	19.7	0.80	
TN8/I_X/11	54	cluster	-24.3	-20.1	16.3	8.7	25.0	25.1	0.78	
TN8/I_X/12	63	cluster	-20.6	-25.1	12.5	9.4	21.9	22.8	0.72	
TN8/G24/4	12	trail	-22.6	-24.7	14.0	9.2	23.3	24.1	0.74	mean: 0.83 range: 0.54–0.94
TN8/G24/5	15	trail	-26.0	-26.8	11.2	13.6	24.8	26.2	0.61	
TN8/G24/4	18	trail	-19.8	-25.3	11.9	9.5	21.4	22.2	0.70	
TN8/G24/6	1	cluster	-21.0	-25.3	12.3	9.9	22.2	23.0	0.70	
TN5/C/5	1	cluster	-25.6	-26.8	11.1	13.4	24.6	25.9	0.61	
TN4/G1/3	5	cluster	-26.3	-21.8	12.8	12.8	25.6	26.4	0.66	
TN4/G1/3	12	cluster	-26.3	-22.9	12.6	12.8	25.4	26.4	0.65	
TN2/X/2	1	trail	-15.7	-28.4	6.8	11.7	18.5	19.2	0.53	
TN2/XX/2	1	trail	-17.3	-26.8	8.9	10.8	19.7	20.4	0.61	

some HCO_3^- should be dissolved in the liquid phase, although it was not detected by micro-Raman analyses on the liquid, likely because it has a low Raman scattering hidden by the Raman bands of quartz (Burke, 2001). Therefore, part of the electrical unbalance could be also related to the presence of unanalysed carbonate minerals (C cannot be quantified by SEM-EDS because of carbon coating) precipitated during thermal decrepitation.

8. Sr isotope analyses on hematite

The results of Sr isotope analyses of the hematite from two veins (TN4H and TN5H) and of two samples of phyllite from the Rio Marina Fm hosting the veins (TN1R and TN2R) are given in Table S4, while the sampling locations are given in Fig. 8a and Table S1. The Sr isotope ratios of the two hematite samples, recalculated at the time of their formation (5.6 Ma), have almost identical $^{87}Sr/^{86}Sr_i$ (0.709219 and 0.709232). These ratios differ significantly from those of the two host rocks (also recalculated at 5.6 Ma), which are variable ($^{87}Sr/^{86}Sr_i$ = 0.713455 and 0.719841) but consistently more radiogenic than hematite.

9. Discussion

The dataset suggests that the fluid circulation and the associated formation of Fe-ore deposits were tightly controlled by the interplay between low-angle normal fault and high-angle oblique-slip transtensional faults, as inferred from the hydrothermal mineral assemblage characterising the damage zones and cataclasite of both fault systems (Figs. 8 and 9). As the analysed faults are minor structures associated with the Zuccale Fault and ENE-striking high-angle oblique slip faults, we can emphasise that these major structures were contemporaneously active, at least during a transient episode, favouring hydrothermal fluid circulation. Similar evidence also comes from other areas of Elba Island (e.g., Liotta et al., 2015; Zucchi et al., 2022), suggesting that a common hydrothermal process characterised this crustal sector, at a depth of ≤6.5 km, as indicated by petrological data (Caggianelli et al., 2018 with references therein). The Fe-ore deposits of the eastern Elba Island were recently dated by Wu et al. (2019), who reported the ages (5.575 ± 0.008 Ma and 5.583 ± 0.013 Ma) of two adularia samples, with essentially flat $^{40}Ar/^{39}Ar$ spectra, and the average (U + Th)/He age of three hematite samples (5.56 ± 0.15 Ma), coexisting with adularia, mostly overlapping with the adularia age. According to these authors, the age of the adularia, estimated by Ar/Ar dating, indicates that the Fe-mineralisation precipitation occurred within a specific age range, between about 5.60–5.57 Ma (taking into account the reported errors in age determinations).

However, the activity of the faults pre-dated and post-dated the deposition of the Fe-ore (Viti et al., 2016; Zucchi et al., 2022), the latter representing a short event that occurred during the extensional process that thinned the lithosphere of the inner Northern Apennines since Burdigalian (Carmignani et al., 1995; Rossetti et al., 2015).

According to Dini et al. (2008b) and Liotta et al. (2015), the high-angle oblique-slip faults can be framed in a NE-trending regional transfer zone, contemporaneous with the extensional tectonics, which controlled the emplacement of the Porto Azzurro monzogranite. This is also supported by the kinematic compatibility between the high-angle NNW- and ENE-striking faults, and the low-angle normal faults of the study area (Fig. 6) and of other localities of Elba (Keller and Pialli, 1990; Duranti et al., 1992; Pertusati et al., 1993; Collettini and Holdsworth, 2004; Collettini et al., 2006; Liotta et al., 2015; Zucchi et al., 2017, 2022).

However, some authors have hypothesized a different scenario for the evolution of the Northern Apennines, the northern Tyrrhenian Basin and magma emplacement. In their view, the extensional tectonics would have played a minor or even no role, whereas compressional tectonics was continuously (or pulsing) active during the Cretaceous-Quaternary time-span (Finetti et al., 2001; Bonini et al., 2014; Viola et al., 2018; Ryan et al., 2021). In our opinion, this view contrasts with first-order evidence, such as the present lithospheric and crustal thickness, geometry, kinematics and P-T evolution of the rock units. However, this issue has been extensively discussed in numerous other papers to which the interested reader is referred (Brogi et al., 2005; Brogi, 2008; Brogi and Liotta, 2008; Liotta et al., 2015; Brogi, 2020; Spiess et al., 2022).

The study area is just located in a sector where cartographic scale high-angle faults dissect the Zuccale Fault and associated minor faults (i.e., low-angle normal faults). It follows that the superposition of faults has resulted in increased permeability, which favours fluid circulation.

The estimated permeability in the hanging wall of the Zuccale Fault is in the order of 10^{-15}–10^{-13} m^2 (Fig. S2c), as obtained by a statistical approach that highlights the most appropriate value by discarding the results from vein length and width analysis that cannot be reasonably explained as an effect of a single deformation event. Overall, the strong relationship between fractures and mineralisation suggests that the efficient porosity follows the trend of secondary permeability, with higher values corresponding to higher fracture aperture and/or the higher fracture density (Fig. S2c).

Nevertheless, the values obtained are comparable to those measured in the Larderello geothermal field (Cappetti et al., 1995; Romagnoli

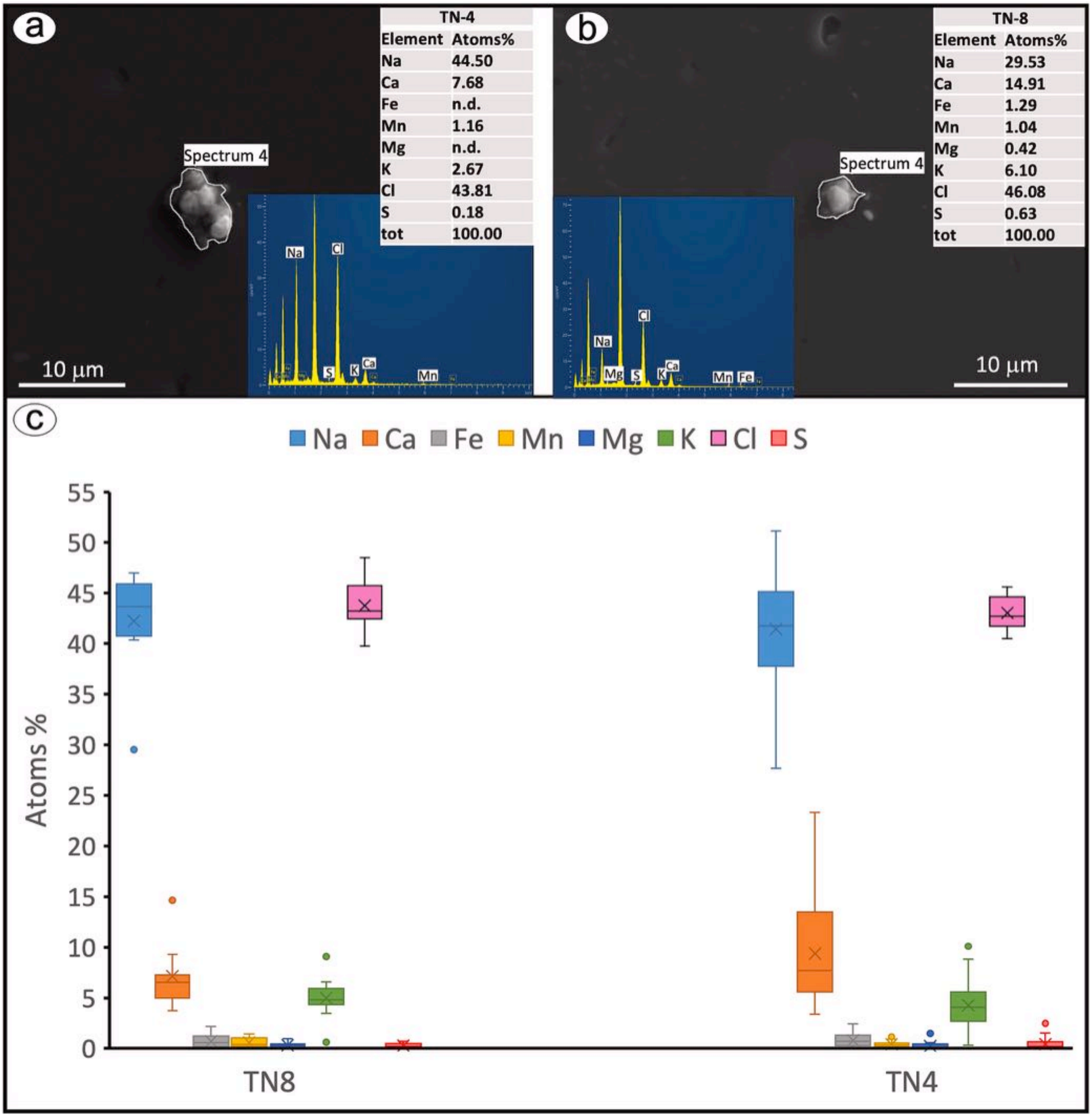

TN-4	
Element	Atoms%
Na	44.50
Ca	7.68
Fe	n.d.
Mn	1.16
Mg	n.d.
K	2.67
Cl	43.81
S	0.18
tot	100.00

TN-8	
Element	Atoms%
Na	29.53
Ca	14.91
Fe	1.29
Mn	1.04
Mg	0.42
K	6.10
Cl	46.08
S	0.63
tot	100.00

Fig. 12. (a,b) SEM images of salt residues resulting from thermal decrepitation, the corresponding EDS spectra (reporting the elements detected in the residues) and computed composition are also shown; (c) box-and-whisker plot (boxplot) of Na, Ca, Fe, Mn, Mg, Cl and S concentrations in the salt residues of TN8 and TN4 samples analysed by SEM-EDS.

et al., 2010), which is considered the current analogue of the eastern Elba Island (Liotta et al., 2021). Furthermore, the fact that comparable permeability values have been obtained in other areas of Elba Island (i.e., Mt. Calamita and Rio Albano areas; Zucchi et al., 2017, 2022), indicates that permeability is maintained constant regardless of the structural level and the chemical-physical properties of the mineralising fluids. This emphasises the role of the active deformation during fluid circulation (Viti et al., 2016) in maintaining an efficient permeability, as opposed to the sealing induced by the fluid-rock interaction.

The evolution of the vein-bearing rocks in the Terranera area, from the emplacement of the Porto Azzurro pluton to the formation of the Fe-ore deposit, is illustrated in Fig. 2. After the emplacement of the monzogranite, dated at 6.53–6.4 Ma (Gagnevin et al., 2011; Spiess et al., 2021), the roof rocks were affected by thermo-metamorphism. Subsequently, a metasomatic process generated a magnesian Fe-skarn in the rocks hosting the Fe-ore deposits. The subsequent formation of low-angle normal faults and high-angle oblique-slip transtensional faults, which crosscut the skarn, favoured the development of a hydrothermal circulation, responsible for the precipitation of the Fe-mineralisation within the veins, at about 5.60–5.57 Ma (Fig. 2).

An estimate of the minimum distance between the mineralised veins and the contact monzogranite complex-roof rock can be obtained by examining the stratigraphic logs of two mine drillings (Fig. 5), located in the hanging wall of the Zuccale Fault. One borehole, drilled in the

Terranera area, found only granitoid dykes at 45.70 and 51.75 m b.s.l., without encountering the monzogranite, down to the bottom of the hole. In contrast, another drill hole about 800 m NW of the Terranera area encountered at least 35 m of a porphyritic granitoid (probably a sill related to the Porto Azzurro monzogranite) from about 275 m b.s.l. to the bottom of the hole (Montecatini, 1950–1953). Thus, considering that the examined samples were collected at 2–5 m a.s.l., it can be assumed that the mineralised veins formed at more than 200–300 m above the roof of the Porto Azzurro monzogranite complex.

The numerical dynamic model of Spiess et al. (2021) describes the cooling and exhumation history, as well as the depth change of the rheological boundaries of the monzogranite and roof rocks for 1 Myr, starting from the magma emplacement at a depth of about 6.5 km. Model results indicate that roof rocks, located at 200–300 m above the pluton, were in the ductile domain, from the start of the thermo-metamorphic event up to about 5.76 Ma (see Fig. 20b of Spiess et al., 2021). In contrast, the rocks were in the brittle domain at the time of deposition of Fe-mineralisation (5.60–5.57 Ma) (Fig. 2). The lithostatic pressure regime likely dominated beneath the ductile domain (Fig. 2). However, the main hydrothermal stage, responsible for the deposition of Fe-mineralisation probably occurred when the fracture networks were fully developed. At this stage, the secondary permeability was relatively high (Fig. S2c), so the system was likely connected to the surface and the hydrostatic pressure regime is assumed to be dominant.

9.1. *Chemical features of the palaeo-geothermal fluids*

Fluid inclusion data show that the geothermal fluid had a multi-component composition. SEM-EDS analyses highlight that the main cations present in the fluid inclusions are Na^+ and subordinately Ca^{++} and K^+ with minor amounts of Fe^{++}, Mn^{++} and Mg^{++} (Fig. 12c and Table S3). Microthermometric data are consistent with the multicomponent nature of the trapped fluids. In fact, the final ice melting temperatures below the eutectic temperature (-21.2 °C) of the H_2O-NaCl system (Table 2) indicate that the composition of the fluid cannot be restricted to a simple H_2O-NaCl binary system. Furthermore, the temperature of the first melting, between approximately -51 and -45 °C, indicates the presence of divalent cations within the fluid (Steele-MacInnis et al., 2016).

Dissolved $B(OH)_3^\circ$ also occurs in the liquid phase of the inclusions, as shown by micro-Raman analyses (Fig. S4b). However, solid H_3BO_3 (i.e., sassolite) was not observed at room temperature or during low temperature microthermometric analyses and never nucleated after laser irradiation during Raman investigations. Therefore, a maximum concentration of $B(OH)_3^\circ$ of 1.9 wt% can be estimated from ice-sassolite or hydrohalite-sassolite cotectic curves in the ternary H_2O-NaCl-H_3BO_3 system, calculated by the Bakker and Schilli (2016) equations, considering the maximum T_{mi} (-14.2 °C) obtained from the examined inclusions.

Raman spectra also showed the presence of CO_2 in the gas phase of some fluid inclusions. However, in most of these inclusions, clathrate was not detected after ice melting. The maximum CO_2 content (0.6 and 0.8 mol% for inclusions in clusters and trails, respectively) was estimated using the mmc2 H_2O-NaCl-CO_2 spreadsheet of Steele-MacInnis (2018) considering: i) the maximum T_{mi} values (-19.7 and -14.2 °C for inclusions in clusters and trails, respectively), ii) the maximum apparent volume % occupied by the bubble at room temperature (25%) and, iii) assuming that clathrate dissociated and ice melted at the same temperature. The maximum CO_2 content (~1.0 mol%) for inclusions showing clathrate dissociation, was calculated using the same spreadsheet, taking into account: i) the maximum clathrate dissociation temperature (-13.4 °C); ii) the T_{mi} (-20.2 °C) of the inclusion exhibiting this dissociation temperature (Table S2) and, iii) an apparent volume of approximately 23% occupied by the bubble.

Salinity of two-phase aqueous inclusions, in which ice is the last solid to melt, can be computed from T_{mi} by applying the formula of Bodnar (1993) for the H_2O-NaCl system. In particular, fluid inclusions in trails are characterised by salinity between 18.0 and 26.6 wt% NaCl eq., whereas fluid inclusions occurring in clusters display a salinity from 22.1 to 26.5 wt% NaCl eq. (Table 2). These values represent an approximation of the true salinity. In fact, it was found that: i) in several inclusions, ice melted at temperatures below the eutectic temperature (-21.1 °C) of the H_2O-NaCl system and salinity was computed by extrapolating the equation of Bodnar (1993) to temperatures below the eutectic point; ii) the examined inclusions contain a multicomponent fluid, including $B(OH)_3^\circ$ and CO_2 dissolved in the liquid phase.

In aqueous CO_2-bearing inclusions in which ice melted in the absence of clathrate, dissolved CO_2 reduces the T_{mi} by up to 1.48 °C (Hedenquist and Henley, 1985). The concentration of dissolved salts for such inclusions is zero, but if salinity is computed from T_{mi} it will be overestimated up to 2.5 wt% NaCl eq. For the examined inclusions, we calculate the highest salinity overestimation (0.8 and 0.7 wt% NaCl eq., for inclusions in clusters and trails, respectively) using the mmc2 H_2O-NaCl-CO_2 spreadsheet of Steele-MacInnis (2018), with the same assumption made for estimating the maximum CO_2 content.

For fluid inclusions with significant concentrations of multiple salts, compositional information can be only obtained if the melting temperature of hydrohalite (and other salts or salt-hydrates), in addition to T_{mi}, can be measured (Steele-MacInnis et al., 2016). In the limited number of the inclusions in which both T_{mi} and T_{mhh} could be measured, it is possible to calculate compositional and total salinity data within the H_2O-NaCl-$CaCl_2$ ternary systems. Indeed, the examined inclusions, mostly contain dissolved NaCl and $CaCl_2$ in the fluid as indicated by SEM-EDS analyses, which showed that Na + Ca represent between 81 and 99% of the cations in the salt residues of decrepitated inclusions (Table S3). The NaCl and $CaCl_2$ concentrations, and total salinity of single inclusions, computed from T_{mi} and T_{mhh} using the spreadsheet of Steele-MacInnis et al. (2011), are shown in Table 3. Specifically, the NaCl and $CaCl_2$ concentrations span from 6.8 to 16.3 and from 5.9 to 13.6 wt%, respectively; with the majority of the inclusions displaying NaCl > $CaCl_2$ concentrations. Total salinity (NaCl wt% + $CaCl_2$ wt%) ranges from 18.5 to 25.6 wt%, while the molar ratio NaCl/(NaCl+$CaCl_2$) is between 0.53 and 0.84 (Table 3). The molar ratio range computed by microthermometry (R_{mol} microth.) largely overlaps the range (0.54–0.94) of the molar ratios calculated from the Na and Ca concentrations (in atoms%) in the salt residues determined by SEM-EDS analyses (R_{mol} SEM-EDS in Tables 3 and S3).

The salinity values calculated in the ternary system differ from the salinity values computed in the H_2O-NaCl system by 0.2–1.4 wt% (Table 3). Thus, in general, the overestimation of the salinity calculated in the H_2O-NaCl system due to the presence of dissolved CO_2 and $CaCl_2$ in the liquid is relatively low compared to the high salinity of the inclusions.

9.2. *Fluid P-T conditions*

The thermo-barometric conditions of the fluid flow can be obtained by combining the data on the depth and age of formation of the mineralised veins (i.e., relation with the granite cooling history) with fluid inclusion isochores. As previously shown, the total salinity of the fluid inclusions can be estimated, in first approximation, from T_{mi} in the H_2O-NaCl system as the CO_2 content in the inclusions is usually relatively low (<0.8 mol%). Thus, the limiting isochores (i.e., minimum and maximum isochores) of fluid inclusions in trails and clusters were computed in the H_2O-NaCl system from the Bodnar and Vityk (1994) data by using the HOKIEFLINCS_H_2O-NaCl spreadsheet of Steele-MacInnis et al. (2012). For this purpose, we used the average T_h and T_{mi} of the FIAs showing the highest and lowest T_h values. The limiting isochores of fluid inclusions in clusters and trails are shown in Fig. 13. A maximum isochore was also computed for an inclusion with a CO_2 content of 0.5 mol%, a salinity of 24.3 wt% NaCl eq., a volume fraction of the carbonic portion of 0.24 and a bulk density of 0.915 g/cm^3, by using the H_2O-NaCl-CO_2 spreadsheet

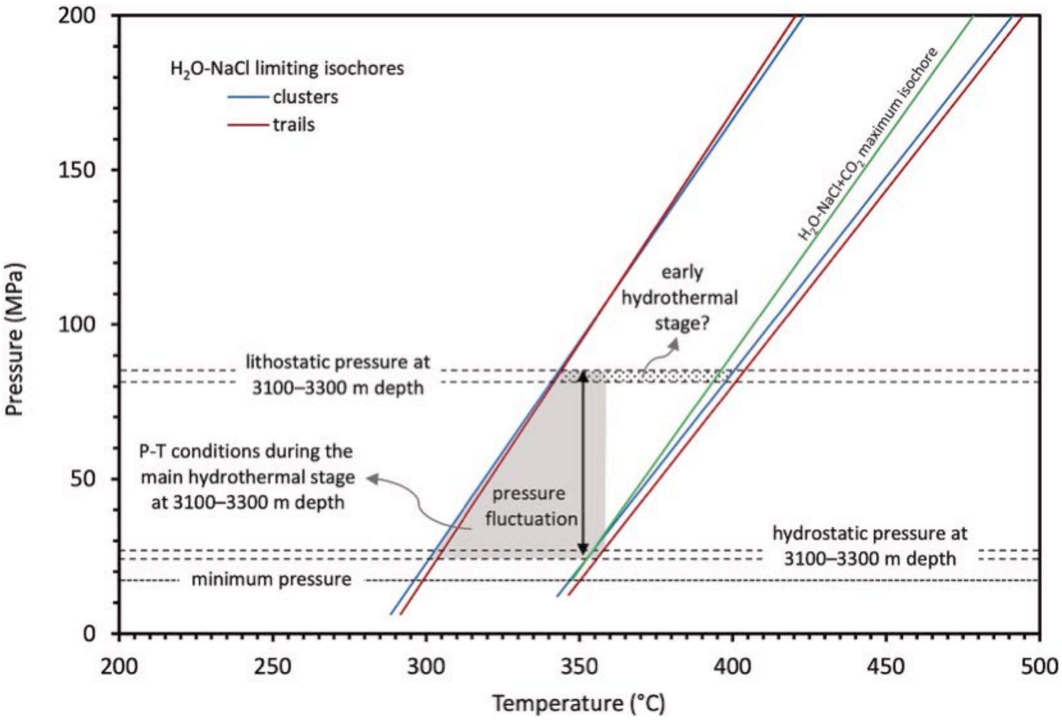

Fig. 13. – P-T diagram showing the limiting isochores of fluid inclusions occurring in trails and clusters computed in the H_2O-NaCl system and a maximum isochore computed in the H_2O-NaCl-CO_2 system. Hydrostatic and lithostatic pressures at 3100–3300 m depth are also shown as well as the minimum pressure (corresponding to the starting point of the H_2O-NaCl-CO_2 isochore). Pressure-temperature trapping conditions of fluid inclusions under the main hydrothermal stage is indicated by the grey field, whereas the dotted field refers to the P-T conditions during a hypothetical early hydrothermal stage. Arrow indicates pressure fluctuations related to local self-sealing causing fluid pressurisation and subsequent depressurisation after hydro-fracturing processes (see text for details).

of Steele-MacInnis (2018). This isochore starts (on the H_2O-NaCl-CO_2 solvus) at about 350 °C and 17 MPa, and it is displayed in Fig. 13 for comparison.

The hydrothermal activity responsible for the formation of quartz-hematite veins developed within the roof rocks of the Porto Azzurro monzogranite pluton during its cooling history. As 200–300 m is the minimum distance from the monzogranite, the estimated maximum depth at which mineralisation occurred is evaluated by the numerical model of Spiess et al. (2021), where the exhumation-time relation of the Porto Azzurro monzogranite is described. Since the radiometric age of adularia associated with the iron mineralisation of Eastern Elba is 5.60–5.57 Ma (Wu et al., 2019) a depth between 3100 and 3300 m b.s.l. (see Fig. 20b of Spiess et al., 2021) can be reasonably estimated. Thus, the pressure range during vein formation must be comprised between lithostatic pressure values of 84–89 MPa (assuming a density of the roof rocks of 2750 kg/m^3) and the hydrostatic pressure values of 28–30 MPa (Fig. 13). The latter were computed based on the average density (about 933 kg/m^3) of the trapped fluids, assuming that the opposite effects on density associated with reducing salinity and temperature within the fluid column towards the surface are equivalent.

The whole range of trapping temperature of inclusions in both clusters and trails at a depth of 3100–3300 m is obtained by the intersections of the lithostatic and hydrostatic pressure values with the limiting isochores (Fig. 13). In particular, the trapping temperatures of fluid inclusions in clusters and trails are comprised between 300 and 400 °C and between 305 and 405 °C, respectively (Fig. 13). The highest values are maximum temperatures as they are computed from the maximum estimated lithostatic pressure values.

By comparing the maximum isochores computed in the H_2O-NaCl and H_2O-NaCl-CO_2 systems, it is evident that the relatively low amount of CO_2 in the examined inclusions has a negligible effect on isochores slope. Conversely, the starting point of the H_2O-NaCl-CO_2 isochore is shifted to a higher pressure (at about 17 MPa) with respect to those of the H_2O-NaCl isochores (Fig. 13). Since the examined inclusions were likely trapped in the liquid field, as suggested by the absence of vapour-rich inclusions, the pressure at the starting point of the H_2O-NaCl-CO_2 isochore represents the minimum pressure during the hydrothermal activity. The depth corresponding to a hydrostatic pressure of 170 MPa, approximately 1900 m, may represent the minimum depth of the hydrothermal system.

The model of Spiess et al. (2021) indicated that rocks hosting the veins at 200–300 m above the pluton were in the brittle domain at the time of Fe-mineralisation formation (5.60–5.57 Ma). As shown above, the main hydrothermal stage likely occurred when the pressure regime was principally at or around hydrostatic values. The position of the limiting isochores of fluid inclusion in cluster and trails is rather close, therefore their intersections with the hydrostatic pressure values at 3100–3330 m depth indicate similar temperature ranges for fluid trapping, between about 300 and 360 °C (Fig. 13).

Fluid inclusions may have been trapped in clusters during quartz growth within the veins, but intense fracturing likely developed microcracks in quartz during and after its growth, allowing the formation of fluid inclusions trails. Although the hydrostatic regime likely predominated, a self-sealing process (i.e., mineral precipitation within veins producing their closure) may have led to a temporary closure of part of the fractures resulting in local pressurisation up to lithostatic values. Subsequent episodes of tectonic and/or hydraulic fracturing and crack propagation increased again permeability and fluid draining away along a rupture zone, as proposed in the fault-valve model, causing depressurisation towards hydrostatic values (Sibson, 1981; Sibson et al., 1988; Sibson, 1990; Boullier and Robert, 1992). Pressure cycling during fluid inclusion trapping (black arrows in Fig. 13) may explain, at least in part, the T_h variation displayed by different FIAs.

The occurrence of hydraulic breccias associated with fault zones (Fig. 9b,c) is consistent with episodic hydro-fracturing processes, associated with fluid pressure cycling, which locally increased the permeability of rock volumes. Similarly, hydraulic brecciation processes are supposed to contribute effectively to the maintenance and enhancement of rock permeability in active geothermal systems, including Larderello (Ruggieri and Gianelli, 1999 and references therein).

Before extensive rock fracturing, the system was not connected to the surface, and a lithostatic or quasi-lithostatic regime is likely to have occurred. Fluid inclusion data do not allow to identify if some inclusions were trapped during an early hydrothermal event at lithostatic conditions. However, if we assume that inclusions in some clusters formed under such conditions, their trapping temperatures may have reached 400 °C (Fig. 13).

The whole possible trapping temperature range (300–405 °C) is comparable to those of fluid inclusions related to the deposition of iron oxides in other Fe-skarn systems during the retrograde hydrothermal stage. For example, the magnetite-hematite ore bodies associated with quartz ± epidote ± calcite ± actinolite in the Andes Cordillera of Southwest Mendoza Province (34°–36°S, Argentina) formed in the temperature range of 290°–436 °C, and temperatures from 300 to 420 °C were estimated for the early retrograde stage of Fe (Cu) skarn deposits in the Sanandaj-Sirjan Belt (NW Iran), during which abundant magnetite precipitated (Franchini et al., 2007; Baghban et al., 2021).

9.3. *Source of the fluids*

The mineralised veins formed through the interaction between hydrothermal fluids and host rocks within the permeable fault zones. The palaeo-geothermal fluid trapped in the inclusions is characterised by rather high salinity values (18.0–26.6 wt% NaCl eq.) and a multicomponent composition (including at least Na, K, Ca, Fe, Mn, Mg, H_3BO_3, Cl, S and CO_2).

Flow of high salinity fluid in the crust can be related to the mobilization of sedimentary formation waters or the occurrence of magmatic-derived brines or generated by halite dissolution (Yardley and Bodnar, 2014).

The involvement of formation waters in the Terranera hydrothermal system can be ruled out because, even if the sedimentary rocks and sediments of the examined area had contained formation waters, they would have been expelled and dispersed during the deformational process of the Northern Apennine orogenesis.

Magmatic-hydrothermal fluids associated with shallow crustal plutons generally show high Na concentrations, subordinately K, Fe, Mn contents and lower Ca amount (Steele-MacInnis et al., 2016). Conversely, fluid resulting from halite dissolution has essentially Na as dissolved cation. However, magmatic- or sedimentary-derived fluids inherit a salinity that reflects their source and origin, and this can be modified through subsequent fluid-rock interactions (Yardley, 2005; Yardley and Bodnar, 2014).

In the examined samples, SEM-EDS analyses showed that the main cation in the evaporates is Na (average: ~42 atoms %) while Ca and K occur in moderate amounts (average: ~8 and ~5 atoms %, respectively), and Fe, Mn and Mg display a lower concentration (Table S3). This suggests that the fluid trapped in the inclusions at Terranera probably did not reflect its original composition but was modified through water-rock interaction processes.

The possibility that the relatively high salinity of the fluids was generated by halite dissolution must be evaluated based on the presence of evaporite deposits in the examined area. Messinian and Upper Triassic evaporite deposits outcrop in the Northern Apennines.

The original Upper Triassic Burano Evaporitic Formation, consisting of alternating gypsum-anhydrite rocks and dolostones, is rarely exposed in the Apennines but is found in boreholes (Martinis and Pieri, 1964; Lugli, 2001). This Formation acted as detachment horizon during the build-up of the Northern Apennines chain and has been affected by severe post-depositional modification and tectonisation; thus, it usually outcrops only as calcareous breccias and cataclasites formed by the removal of the sulphate portion (Boccaletti et al., 1987; Carmignani and Kligfield, 1990; Lugli, 2001). Halite horizons are only rarely found in some boreholes, although Lugli (2001) suggests subsurface dissolution of halite to form thick matrix-supported residual caprock-like, anhydrite mega-breccias. In the examined area, the Burano Formation consists of dolostones or occurs in the form of calcareous breccias and cataclasites (Calcare Cavernoso Auctt.), whereas sulphates or halite horizons belonging to Messinian and Upper Triassic evaporite deposits were never observed in outcrops, in mining explorative drillings and in offshore boreholes (Montecatini, 1950–1953; Bortolotti et al., 2001; Cornamusini and Pascucci, 2014). Thus, the salinity of the fluid at Terranera is unlikely derived from halite dissolution.

The most probable explanation for the relatively high salinity in the Terranera fluid is, therefore, the flow of a fluid exsolved from a magma. However, its multicomponent composition may not be an original feature but likely related to fluid-rock interactions. In particular, the relatively high Ca content in fluid inclusions can be explained by the dissolution of carbonate rock along the flow path. Such a process was also suggested, for example, by Samson et al. (2008) to explain the elevated concentration of Ca in fluid inclusions of the Zn-Pb-Ag skarns of El Mochito (Honduras). Carbonate rocks outcrop in the area of Terranera as embedded in the damage zone of the Zuccale Fault and are also reported in the stratigraphic logs of some mining explorative drillings (Montecatini, 1950–1953). Garofalo et al. (2023) proposed that the magnesian skarn associated with the Zuccale Fault at Terranera formed through the interaction of hydrothermal fluids and dolomitic protolith. The Mg content determined by SEM-EDS analyses in the salt residues of decrepitated inclusions is always low compared to the Ca content (Fig. 12c, Table S3), suggesting that fluid-dolomite interaction cannot directly explain the relatively high Ca content in the inclusions. However, it is possible that the metasomatic processes during Mg-skarn formation consumed most of the Mg present in the system, leaving Ca in the relatively high salinity residual fluid that circulated in the quartz-hematite veins.

Isotopic Sr results provide clear evidence that the magmatic-derived fluid interacted with carbonates. In fact, in Fig. 14 the initial Sr isotope

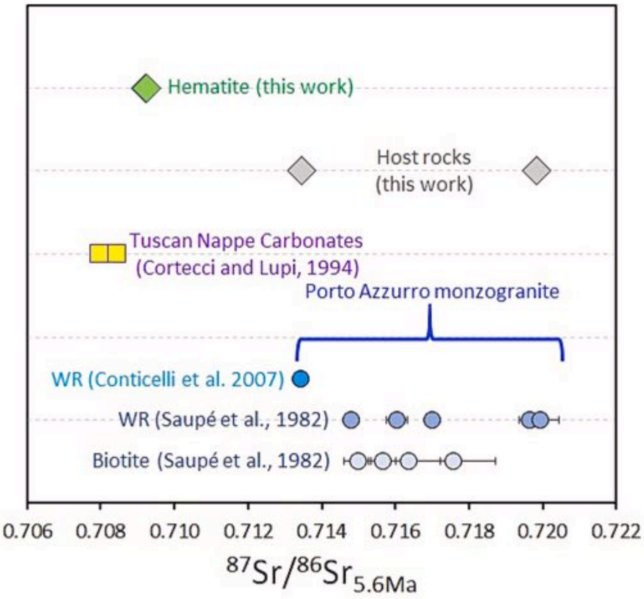

Fig. 14. – Sr isotope composition of the studied hematite separates (TN4H and TN5H) and host rocks (TN1R and TN2R), compared to possible Sr sources related either to the fluid origin (Porto Azzurro pluton, data from Conticelli et al., 2007 and Saupé et al., 1982) or fluid-rock interaction with carbonates (Cortecci and Lupi, 1994). When not visible, errors are smaller than the symbols.

ratios of hematite are compared with those of the host rocks (phyllite of Rio Marina Fm), as well as other possible sources for the Sr carried by the hydrothermal fluids, namely from the Porto Azzurro monzogranite (Saupé et al., 1982; Conticelli et al., 2007) and carbonates (Cortecci and Lupi, 1994), all recalculated at the time of the vein formation (5.6 Ma).

The figure shows that the Sr isotope composition of the hematite, and thus of the hydrothermal fluids, cannot be derived solely from that of the host rocks or from a fluid exsolved from the Porto Azzurro pluton. On the contrary, it requires a dominant contribution from a less radiogenic source, most likely represented by the carbonates embedded in the Zuccale fault zone, likely encountered by the hydrothermal fluids. Carbonates have slightly less radiogenic $^{87}Sr/^{86}Sr_i$ than hematite (both recalculated at 5.6 Ma), indicating that the Sr carried by the hydrothermal fluids must derive from two (or more) sources, including the Porto Azzurro monzogranite, the carbonates and possibly also the host rocks. Simple mass balance considerations indicate that >80% of the Sr in the fluids must be derived from carbonates. Moreover, fluid-carbonate rock interaction processes can have also generated the CO_2 occurring in the trapped fluid. It cannot be also excluded that graphite contained in the meta-sediments of the Rio Marina Fm at Terranera produced CO_2 during the hydrothermal activity. Similarly, a contribution of magmatic CO_2 cannot be ruled out.

On the other hand, boron can be inherited from the original magmatic fluid. Indeed, the circulation of late magmatic boron-bearing fluid within and around the Porto Azzurro monzogranite intrusion is also testified by the frequent occurrence of tourmaline ± quartz veins crosscutting the monzogranite and the micaschist roof rocks (Dini et al., 2008b; Zucchi et al., 2017; Spiess et al., 2021). In particular, Zucchi et al. (2017) reported that in these veins, hosted in the micaschist exposed in south-eastern Elba Island, two-phase liquid inclusions in tourmaline are characterised by rather high T_h (up to 540 °C) and salinities (up to 25.5 wt% NaCl eq.).

Experiments on fluid-rock interaction between Elba Island micaschist and boron-bearing aqueous fluid resulted in the dissolution of biotite of the micaschist of the Mt. Calamita Fm, the precipitation of tourmaline and significant Fe enrichment in the reacted fluid (Orlando et al., 2017). Thus, at least part of the Fe present in the fluid of the Terranera hydrothermal system may have originated from this reaction.

High-salinity Na-rich fluid inclusions containing significant amounts of Ca, K, Fe, and Mn were similarly found in deposits and mineralisation related to magmatic fluid in granitic environments, for example in the Th-U-REE mineralisation of Capitan Mountains (New Mexico, USA), in the Cligga Head Sn–W deposit (SW England) and in the Sn-Zn-Cu-Ag deposit of East Kemptville (Nova Scotia, Canada) (Campbell et al., 1995; Smith et al., 1996, b; Kontak, 2004).

Finally, the T_h vs. salinity diagram of Fig. 15 shows that although fluid inclusions in both clusters and trails have similar T_h ranges and, in most cases, also similar salinity values, a number of inclusions in trails are characterised by somewhat lower salinity values. Most of these inclusions occur along trails crosscutting the quartz edges. Thus, the lower salinity values of such inclusions can be likely related to an input of limited amounts of low-salinity fluid, likely of meteoric origin, which diluted the saline fluid of magmatic origin during the late stage of hydrothermal activity.

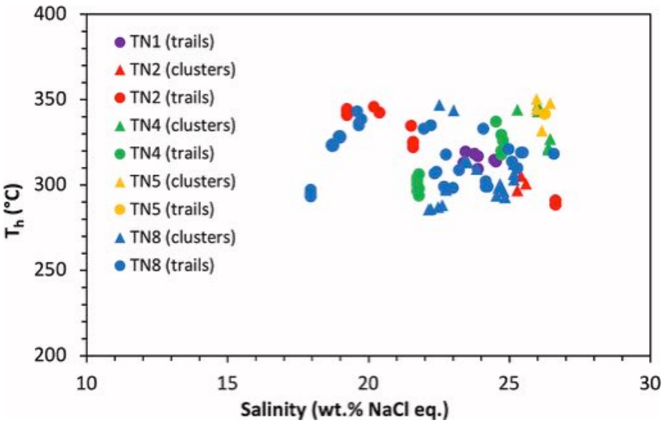

Fig. 15. (a) Salinity vs. homogenisation temperature (T_h) diagram for fluid inclusions in trails and clusters.

9.4. Fe-mineralisation fluid inclusion data vs. Larderello geothermal fluids

Microthermometric data on fluid inclusions in the Terranera and Rio Marina Fe-mineralisation have been reported by Dünkel (2002). In particular, the application of infrared (IR) microscopy to the study of fluid inclusions in hematite allowed to observe the melting of of ice (or hydrohalite) between -30.7 and -26.7 °C and the T_h from 298.9 to 330.7 °C (Table 6.1 in Dünkel, 2002). Such T_h values are within the T_h range of the inclusions trapped in quartz. The melting temperatures are lower than or equal to the lowest T_{mi} (-26.7 °C) and T_{mhh} (-28.4 °C) of our examined fluid inclusions in quartz. The difference in melting temperature may be related to a slightly higher salinity of the fluid trapped in hematite. Moreover, Dünkel (2002) reported the additional melting of a second phase with temperatures of −11.8 and -9.9 °C. This phenomenon was interpreted as either metastable melting (of ice?) or an effect of the presence of iron chloride in the fluid inclusions. Some of the inclusions examined in the present work also showed the melting of a phase between -17.8 and -13.4 °C, after T_{mi} and/or T_{mhh}. This phase is identified as clathrate on the basis of the presence of CO_2 in the inclusions, as revealed by the micro-Raman analyses. It should be noted that the SEM-EDS analyses indicate that Fe is present in relatively small amounts in the evaporates (<2.5 atoms%, Fig. 12), implying a rather low concentration of this element in the fluid inclusions, compared to the other elements. Thus, considering the high solubility of iron chlorides (Lecumberri-Sanchez et al., 2015), it seems unlikely that such solids can be observed in the examined inclusions.

The study of Garofalo et al. (2023) of skarn and hydrothermal alteration occurring in the Zuccale Fault, reports fluid inclusion data form samples of quartz-goethite (+ hematite, magnetite and clays) extensional veins that are in part comparable to our data. In particular, this study identifies two types of inclusions: one, with relatively high salinity (total salinity from 21.8 to 26.3 wt% of $NaCl+CaCl_2$) and another, in which NaCl is the dominant dissolved salt in the fluid characterised by lower salinity (between 1.6 and 13.3 wt% NaCl). These two fluid types circulated and mixed in the Zuccale Fault. The chemical characteristics of the first type, as well as its T_h range (286–329 °C), are comparable to those of the inclusions found in our examined samples. Moreover, although our inclusions do not record the occurrence of the low-salinity fluid, they show a moderate variation in salinity, which is interpreted as the result of a mixing process between fluids of different salinities, similar to that proposed by Garofalo et al. (2023).

The pressure and temperature ranges, as estimated by Garofalo et al. (2023) for the hydrothermal circulation in the quartz-goethite, are 27–125 MPa and 180–350 °C, respectively. The pressure range largely overlaps with the trapping pressure (28–89 MPa) of our fluid inclusions, while their temperature range is somewhat wider but still consistent for the highest values with our fluid inclusion trapping temperature range (300–360 °C) during the main hydrothermal stage.

Deschamps et al. (1983) reported data on fluid inclusions in quartz from the Fe-deposit of Valle Giove located about 1 km NNW of Rio Marina (Fig. 1b). This deposit shares several geological-structural and mineralogical features with Terranera (Zucchi et al., 2022). In addition, the fluid inclusion data are in part similar to those of the fluid inclusions found at Terranera. Indeed, fluid inclusions from Valle Giove showed T_h values mostly between 250 and 350 °C (Fig. 11 of Deschamps et al., 1983) with relatively small amounts of CO_2 (<1.8 mol%). On the other hand, with regard to T_{mi}, some inclusions from Valle Giove, show relatively low values (from -28.7 to -27.9 °C) quite similar to those of Terranera, but others are characterised by higher values (from -13.5 to -7.0 °C). This could be related to a greater dilution of the saline fluid of magmatic origin by low saline meteoric water in the Valle Giove hydrothermal system. Therefore, the mineralising fluids in the Terranera and Valle Giove deposits were partially similar and probably flowed under comparable P-T conditions.

The palaeo-geothermal fluids that circulated at Terranera are very different from those currently found in the Larderello geothermal field, which produce superheated steam and minor gases consisting mainly of CO_2 and H_2S (Batini et al., 2003).

However, studies of fluid inclusions trapped in minerals occurring in metamorphic and igneous rocks cored at depths >2500 m in some Larderello geothermal wells indicated that the past fluid circulation in this system was characterised by multiple fluid types (i.e. magmatic, contact-metamorphic, meteoric) and a complex sequence of fluid trapping during P-T evolution (Cathelineau et al., 1994; Boiron et al., 2007, and references therein). In particular, such studies have shown that relatively high salinity fluids with a multicomponent composition (similar to those found at Terranera) flowed during the past hydrothermal activity at Larderello, supporting the analogy between the fossil (Elba Island) and the active (Larderello) geothermal systems. However, the temperatures of such fluids at Larderello are higher (425–650 °C) than those of the fluids that flowed at Terranera (300–405 °C), probably because at Larderello the fluid inclusions were trapped at higher lithostatic pressures (100–130 MPa) and consequently at greater depths.

9.5. Model of the palaeo-geothermal fluid circulation

During the extensional tectonics (Miocene), low- and high-angle normal faults were developed by mineralising events in which fault zones and especially transfer faults played a fundamental role in channelling hot fluids (Fig. 16). The whole data suggest that the geothermal fluids responsible for Fe-mineralisation are comparable to those that circulated along the Zuccale Fault and then migrated along first generation low- and high-angle faults. The contemporaneity of first generation low- and high-angle normal faults is evidenced by the hydrothermal mineral assemblage developed in their respective cataclasite.

Other parameters being equal (i.e., fracture interconnectivity, fluid viscosity and density, temperature, among others), permeability through fractures is a consequence of the fault kinematics, thus of the attitude of the intermediate stress axis, assuming parallelism between kinematic and stress axes (Sibson, 2000; Faulkner and Armitage, 2013). As a consequence, strike to oblique-slip faults have the intermediate stress axis near vertical, whereas normal faults have a horizontal intermediate axis (Anderson, 1951). In terms of permeability, this implies that deep fluids can be more easily channelled to the surface if they have flowed through strike or oblique-slip faults, thus maintaining their original temperature. We therefore expect this to be the case for the NNW- and NNE-trending faults analysed (Figs. 1 and 6). On the other hand, these latter faults, which play the role of transfer faults, are geometrically linked to the coeval normal faults, where the most favourable permeability is horizontal or close to it. This implies that the fluids flowing up the transfer faults can migrate laterally into the

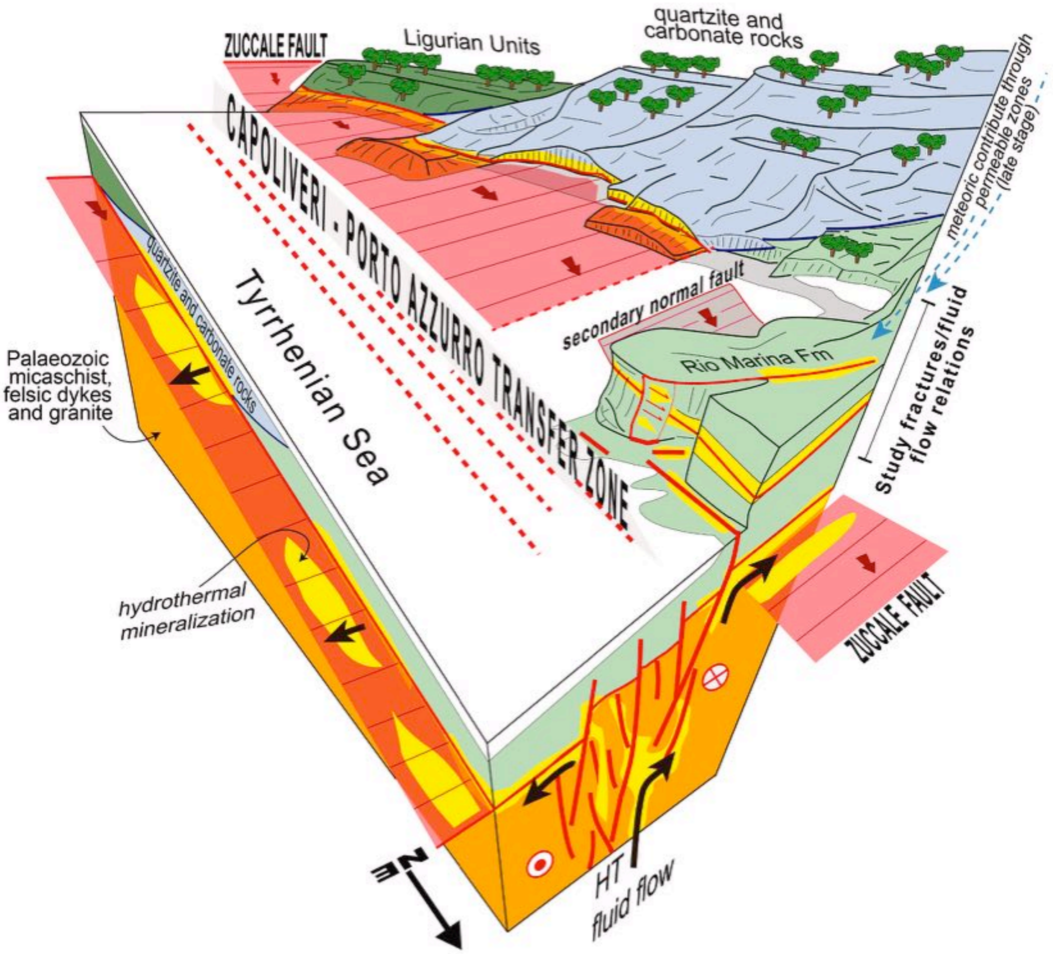

Fig. 16. Conceptual model, not to scale, displaying the relationships between the Zuccale Fault and the Capoliveri-Porto Azzurro transfer zone. This latter represents the main pathway for the upflow of the geothermal fluids under study. Mixing of meteoric water is also considered during the final stage of exhumation and uplift.

permeable damage zone of the normal faults, if the two are hydraulically (and geometrically) connected.

Thus, considering that the hydrothermal system, active between 5.60 and 5.57 Ma, was characterised by the circulation of saline fluids of magmatic origin, these could have exsolved at an earlier stage and remained trapped at depth under a ductile regime, until the cooling allowed the formation of fractures and then the migration of the fluid towards the shallow parts of the system, under a prevailing hydrostatic regime, where they interacted with carbonates and locally mixed with low-salinity meteoric fluids during the late stage of hydrothermal activity.

10. Conclusions

The integrated methodological approach applied in the study area allows us to define how hot to super-hot palaeo-geothermal fluids circulated in an extensional regime, and in particular in a volume of rocks affected by normal and transfer faults. Faults have played a fundamental role in the channelling of palaeo-fluids, as highlighted by: (i) the fracture networks and (ii) the hydrothermal minerals that fill the fractures in the damaged volumes. Fracture networks have progressively increased the secondary permeability, as evidenced by the estimated permeability values associated with to the low- and high-angle faults, which are consistent with those obtained in active geothermal systems and in particular those of the first reservoir exploited in the Larderello geothermal area.

The hydrothermal activity responsible for the formation of the quartz-hematite veins at Terranera developed within the roof rocks of the Porto Azzurro monzogranite pluton, at a maximum depth of c. 3100–3300 m b.s.l., under brittle conditions. The hydrothermal fluids were saline (18.0–26.6 wt% NaCl eq.), mainly of magmatic origin, and their composition is characterised by the presence of Na, Ca, K and Cl with minor amounts of Fe, Mn, Mg, S, B(OH)$_4^-$ and CO_2.

Some components (i.e., Ca, Sr, Fe, CO_2) can be incorporated by interaction of the magmatic fluid with the rocks (carbonate rocks and phyllite) encountered along its path. Mixing processes between the saline fluid and low-salinity fluid, likely of meteoric origin, resulted in a decrease in salinity during the late stage of fluid circulation. The main hydrothermal stage developed under prevailing hydrostatic pressure (28–30 MPa) at a temperature between 300 and 360 °C, whilst a maximum temperature around 400 °C was estimated prior to this stage, assuming lithostatic pressure (89 MPa). Transient, local fluid pressurisations, due to self-sealing process and subsequent drops down to hydrostatic values, probably occurred during hydraulic brecciation. The geological-structural, mineralogical, and fluid inclusions characteristics of Terranera are broadly comparable to those of the Fe-deposits of Valle Giove (Rio Marina), suggesting that the two systems developed under similar conditions.

In conclusion, the study of hot to super-hot palaeo-fluids and their distribution through fractures, has shed light on the structural conditions to be investigated in active geothermal systems to decrease the mining risk during exploration. Fossil system studies are therefore essential to assessing the geothermal potential of any prospective area.

Supplementary data to this article can be found online at https://doi.org/10.1016/j.tecto.2024.230210.

CRediT authorship contribution statement

Martina Zucchi: Writing – review & editing, Writing – original draft, Software, Methodology, Investigation, Formal analysis, Data curation, Conceptualization. **Andrea Brogi:** Writing – review & editing, Writing – original draft, Validation, Methodology, Data curation, Conceptualization. **Domenico Liotta:** Writing – review & editing, Writing – original draft, Validation, Conceptualization. **Rosa Anna Fregola:** Writing – review & editing, Writing – original draft, Formal analysis. **Alfredo Caggianelli:** Writing – review & editing, Validation, Formal analysis. **Gennaro Ventruti:** Writing – review & editing, Formal analysis. **Riccardo Avanzinelli:** Writing – review & editing, Methodology, Formal analysis. **Giovanni Ruggieri:** Writing – review & editing, Writing – original draft, Validation, Formal analysis, Data curation.

Declaration of competing interest

The authors declare that they have no known competing financial interests or personal relationships that could have appeared to influence the work reported in this paper.

Data availability

Data will be made available on request.

Acknowledgments

The research leading to these results has received funding from the European Community's Seventh Framework Programme under grant agreement No. 608553 (Project IMAGE). M.Z. received funding from the Italian Ministry of University and Research (MIUR), through the program PON-AIM (Attraction and International Mobility) – project no. 1815472, Activity 1, line 1. We are grateful to Andrea Dini for fruitful discussions on the topic here presented and to Chiara Maccelli for help in the sample preparation for the Sr isotope measurements. We are warmly grateful to the Editor Samuel Angiboust and to Bruce Yardley, Gaston Godard and two other anonymous reviewers for their constructive comments, which helped us to improve the original manuscript.

References

Acocella, V., Funiciello, R., 2006. Transverse systems along the extensional Tyrrhenian margin of Central Italy and their influence on volcanism. Tectonics 25. https://doi.org/10.1029/2005TC001845.

Alaniz-Álvarez, S.A., Nieto-Samaniego, Á.F., Morán-Zenteno, D.J., Alba-Aldave, L., 2002. Rhyolitic volcanism in extension zone associated with strike-slip tectonics in the Taxco region, southern Mexico. J. Volcanol. Geotherm. Res. 118, 1–14. https://doi.org/10.1016/S0377-0273(02)00247-0.

Alçiçek, H., Bülbül, A., Brogi, A., Liotta, D., Ruggieri, G., Capezzuoli, E., Meccheri, M., Yavuzer, I., Alçiçek, M.C., 2018. Origin, evolution and geothermometry of thermal waters in the Gölemezli geothermal field, Denizli Basin (SW Anatolia, Turkey). J. Volcanol. Geotherm. Res. 349, 1–30.

Alt-Epping, P., Diamond, L.W., HarinG, M.O., 2013. Prediction of water-rock interaction and porosity evolution in a granitoid hosted enhanced geothermal system, using constraints from the 5 km Basel-1 well. Appl. Geochem. 38, 121–133.

Anderson, E.M., 1951. The Dynamics of Faulting and Dike Formation with Application to Britain, 2nd edition. Oliver and Boyd (Edinburgh, 133147).

Ármannsson, H., Fridriksson, T., Benjamínsson, J., Hauksson, T., 2015. History of Chemical Composition of Geothermal Fluids in Krafla, Northeast Iceland, with Special Emphasis on the Liquid Phase. Proceedings World Geothermal Congress 2015, Melbourne, Australia, 19–25 April 2015, pp. 1–7.

Baghban, S., Zandi, Z., Lentz, D.R., 2021. Formation and evolution of the calcic-magnesian Saheb Fe(Cu) skarn deposit from the Sanandaj-Sirjan Belt, NW Iran: evidence for multistage boiling in episodes of magnetite saturation. J. Geochem. Explor. 226, 106781.

Bakker, R.J., Schilli, S.E., 2016. Formation conditions of leucogranite dykes and aplite-pegmatite dykes in the eastern Mt. Capanne plutonic complex (Elba, Italy): Fluid inclusion studies in quartz, tourmaline, andalusite and plagioclase. Mineral. Petrol. 110, 43–63.

Baldi, P., Bertini, G., Cameli, G.M., Decandia, F.A., Dini, I., Lazzarotto, A., Liotta, D., 1994. La tettonica distensiva post-collisionale nell`area geotermica di Larderello (Toscana meridionale). Studi Geol. Camerti 1, 183–193.

Barchi, M.R., 2010. The neogene-quaternary evolution of the Northern Apennines: Crustal structure, style of deformation and seismicity. In: Beltrando, M., Peccerillo, A., Mattei, M., Conticelli, S., Doglioni, C. (Eds.), The Neogene-Quaternary Evolution of the Northern Apennines: Crustal Structure, Style of Deformation, Seismicity, 36. Journal of the Virtual Explorer. https://doi.org/10.3809/jvirtex.2009.00220.

Bartole, R., 1995. The North Tyrrhenian-Northern Apennines post-collisional system: constraints for a geodynamic model. Terra Nova 7, 7–30.

Batini, F., Brogi, A., Lazzarotto, A., Liotta, D., Pandeli, E., 2003. Geological features of the Larderello-Travale and Mt. Amiata geothermal areas (southern Tuscany, Italy). Episodes 26, 239–244.

Baumgartner, M., Bakker, R.J., 2009. $CaCl_2$-hydrate nucleation in synthetic fluid inclusions. Chem. Geol. 265, 335–344.

Bianco, C., Brogi, A., Caggianelli, A., Giorgetti, G., Liotta, D., Meccheri, M., 2015. HP-LT metamorphism in Elba Island: implications for the geodynamic evolution of the inner Northern Apennines (Italy). J. Geodyn. 91, 13–25.

Bianco, C., Godard, G., Halton, A., Brogi, A., Liotta, D., Caggianelli, A., 2019. The lawsonite-glaucophane blueschists of Elba Island (Italy). Lithos 348–349, 105198.

Boccaletti, M., Decandia, F.A., Gasperi, G., Gelminini, R., Lazzarotto, A., Zanzucchi, G., 1987. Note illustrative della carta strutturale dell'Appennino Settentrionale. CNR 429-1982, 203.

Bodnar, R.J., 1993. Revised equation and table for determining the freezing point depression of H_2O-NaCl solutions. Geochim. Cosmochim. Acta 57, 683–684.

Bodnar, R.J., Vityk, M.O., 1994. Interpretation of microthermometric data for H_2O-NaCl fluid inclusions. In: De Vivo, B., Frezzotti, M.L. (Eds.), Fluid Inclusions in Minerals, Methods and Applications. Virginia Tech, Blacksburg, pp. 117–130.

Boiron, M.C., Cathelineau, M., Ruggieri, G., Jeanningros, A., Gianelli, G., Banks, D.A., 2007. Active contact metamorphism and CO_2–CH_4 fluid production in the Larderello geothermal field (Italy) at depths between 2.3 and 4 km. Chem. Geol. 237, 303–328.

Bonini, M., Sani, F., Stucchi, E.M., Moratti, G., Benvenuti, M., Menanno, G., Tanini, C., 2014. Late Miocene shortening of the Northern Apennines back-arc. J. Geodyn. 74, 1–31.

Bortolotti, V., Fazzuoli, M., Pandeli, E., Babbini, A., Corti, S., 2001. Geology of central and eastern Elba Island. Ofioliti 26, 97–150.

Boullier, A.M., Robert, F., 1992. Palaeosismic events recorded in Archean gold–quartz vein networks, Val d'Or, Abitibi, Quebec, Canada. J. Struct. Geol. 14, 161–179.

Brhun, R.L., Gibler, P.R., Parry, W.T., 1987. Rupture characteristics of normal faults: an example from the Wasatch fault zone, Utah. Geol. Soc. Lond. 28, 337–353. https://doi.org/10.1144/GSL.SP.1987.028.01.21.

Brogi, A., 2004. Miocene low-angle detachments and upper crust megaboudinage in the Mt. Amiata geothermal area (Northern Apennines, Italy). Geodin. Acta 17, 375–387.

Brogi, A., 2008. Kinematics and geometry of Miocene low-angle detachments and exhumation of the metamorphic units in the hinterland of the Northern Apennines (Italy). J. Struct. Geol. 30, 2–20.

Brogi, A., 2020. Late evolution of the inner Northern Apennines from the structure of the Monti del Chianti-Monte Cetona ridge (Tuscany, Italy). J. Struct. Geol. 141, 104205 https://doi.org/10.1016/j.jsg.2020.104205.

Brogi, A., Fulignati, P., 2012. Tectonic control on hydrothermal circulation and fluid evolution in the Pietratonda-Poggio Peloso (southern Tuscany, Italy) carbonate-hosted Sb-mineralization. Ore Geol. Rev. 44, 158–171.

Brogi, A., Liotta, D., 2008. Highly extended terrains, lateral segmentation of the substratum, and basin development: the middle-late Miocene Radicondoli Basin (inner northern Apennines, Italy). Tectonics 27, TC5002. https://doi.org/10.1029/2007TC002188.

Brogi, A., Lazzarotto, A., Liotta, D., Ranalli, G., 2005. Crustal structures in the geothermal areas of southern Tuscany (Italy): insights from the CROP 18 deep seismic reflection lines. J. Volcanol. Geotherm. Res. 148, 60–80.

Brogi, A., Alçiçek, M.C., Liotta, D., Capezzuoli, E., Zucchi, M., Matera, P.F., 2021. Step-over fault zones controlling geothermal fluid-flow and travertine formation (Denizli Basin, Turkey). Geothermics 89, 101941. https://doi.org/10.1016/j.geothermics.2020.101941.

Burke, E.A.J., 2001. Raman microspectrometry of fluid inclusions. Lithos 55, 139–158.

Caggianelli, A., Ranalli, G., Lavecchia, A., Liotta, D., Dini, A., 2014. Post-emplacement thermo- rheological history of a granite intrusion and surrounding rocks: The Monte Capanne pluton, Elba Island, Italy. In: Llan-Fúnez, S., Marcos, A., Bastida, F. (Eds.), Deformation Structures and Processes within the Continental Crust. Geological Society, London. https://doi.org/10.1144/SP394.1. Special Publications 394.

Caggianelli, A., Zucchi, M., Bianco, C., Brogi, A., Liotta, D., 2018. Estimating P-T metamorphic conditions on the roof of a hidden granitic pluton: an example from the Mt. Calamita promontory (Elba Island, Italy). Ital. J. Geosci. 137, 238–253.

Calcagnile, G., Panza, G.F., 1981. The main characteristics of the Lithosphere Asthenosphere System in Italy and surrounding regions. Pure Appl. Geophys. 119, 865–879.

Campbell, A.R., Banks, D.A., Phillips, R.S., Yardley, B.W.D., 1995. Geochemistry of Th-U-REE mineralizing magmatic fluids, Capitan Mountains, New Mexico. Econ. Geol. 90, 1271–1287.

Cappetti, G., Parisi, L., Ridolfi, A., Stefani, G., 1995. Fifteen years of reinjection in the Larderello-Valle Secolo area: analysis of the production data. In: Florence, Italy, May 18–31. Proceedings World Geothermal Congress WGC95, vol. 3, pp. 1797–2000.

Carmignani, L., Kligfield, R., 1990. Crustal extension in the northern Apennines: the transition from compression to extension in the Alpi Apuane core complex. Tectonics 9, 1275–1303.

Carmignani, L., Decandia, F.A., Fantozzi, P.L., Lazzarotto, A., Liotta, D., Meccheri, M., 1994. Tertiary extensional tectonics in Tuscany (northern Apennines, Italy). Tectonophysics 238, 295–315.

Carmignani, L., Decandia, F.A., Disperati, L., Fantozzi, P.L., Lazzarotto, A., Liotta, D., Oggiano, G., 1995. Relationships between the Tertiary structural evolution of the Sardinia-Corsica-provençal domain and the northern Apennines. Terra Nova 7, 128–137.

Cassinis, R., Scarascia, S., Lozej, A., 2003. The deep crustal structure of Italy and surrounding areas from seismic refraction data; a new synthesis. Ital. J. Geosci. 122, 365–376.

Cathelineau, M., Marignac, C., Boiron, M.C., Gianelli, G., Puxeddu, M., 1994. Evidence for Li-rich brines and early magmatic fluid rock interaction in the Larderello geothermal system. Geochim. Cosmochim. Acta 58, 1083–1099.

Chmielowski, J., Zandt, G., Haberland, C., 1999. The central Andean Altiplano-Punamagma body. Geophys. Res. Lett. 26 (6), 783–786. https://doi.org/10.1029/1999GL900078.

Collettini, C., Barchi, M.R., 2004. A comparison of structural data and seismic images for low-angle normal faults in the Northern Apennines (Central Italy): constraints on activity. Geol. Soc. Lond. Spec. Publ. 224, 95–112. https://doi.org/10.1144/GSL.SP.2004.224.01.07.

Collettini, C., Holdsworth, R.E., 2004. Fault zone weakening processes along low-angle normal faults: insights from the Zuccale Fault, Isle of Elba, Italy. J. Geol. Soc. Lond. 161, 1039–1051.

Collettini, C., De Paola, N., Goulty, N.R., 2006. Switches in the minimum compressive stress direction induced by overpressure beneath a low-permeability fault zone. Terra Nova 18, 224–231. https://doi.org/10.1111/j.1365-3121.2006.00683.x.

Collettini, C., Viti, C., Smith, S.A.F., Holdsworth, R.E., 2009. Development of interconnected talc networks and weakening of continental low-angle normal faults. Geology 37, 567–570.

Conticelli, S., Bortolotti, V., Principi, G., Laurenzi, M.A., D'Antonio, M., Vaggelli, G., 2007. Petrology, mineralogy and geochemistry of the mafic dike from Monte Castello, Elba Island, Italy. Ofioliti 26 (2a), 249–262.

Cornamusini, G., Pascucci, V., 2014. Sedimentation in the Northern Apennines-Corsica tectonic knot (Northern Tyrrhenian Sea, Central Mediterranean): offshore drilling data from the Elba-Pianosa ridge. Int. J. Earth Sci. 103, 821–842.

Cortecci, G., Lupi, L., 1994. Carbon, oxygen and strontium isotope geochemistry of carbonates rocks from the Tuscan Nappe, Italy. Mineral. Petrogr. Acta 37, 63–80.

Cox, S.F., 1999. Deformational controls on the dynamics of fluid flow in mesothermal gold systems. Geol. Soc. Lond. Spec. Publ. 155, 123–140.

Creixell, C., Parada, M.Á., Roperch, P., Morata, D., Pérez de Arce, C., 2006. Syn-tectonic emplacement of the Middle Jurassic Concón Mafic Dike Swarm, Coastal Range, Central Chile (33° S). Tectonophysics 425 (1–4), 101–122.

Curewitz, D., Karson, J.A., 1997. Structural settings of hydrothermal outflow: fracture permeability maintained by fault propagation and interaction. J. Volcanol. Geotherm. Res. 79, 149–168.

Daniel, J.M., Jolivet, L., 1995. Detachment faults and pluton emplacement: Elba Island (Tyrrhenian Sea). Bulletin de la Société Géologique de France 166, 341–354.

Deschamps, Y., Gagallier, G., Macaudière, J., Marignac, C., Moine, B., Saupé, F., 1983. Le gisement de pyrite-hematite de Valle Giove (Rio Marina, Ile d'Elbe, Italie) (Constribution à la connaissance des gisements de Toscane - I). Schweizer Mineralogische Petrographische Mitteilungen, 63, 301–327.Dini, A., 2003. Ore deposits, industrial minerals and geothermal resources. Per. Mineral. 72, 41–52.

Dini, A., 2003. Ore deposits, industrial minerals and geothermal resources. Periodico di Mineralogia 72, 41–52.

Dini, A., Gianelli, G., Puxeddu, M., Ruggieri, G., 2005. Origin and evolution of Pliocene–Pleistocene granites from the Larderello geothermal field (Tuscan Magmatic Province, Italy). Lithos 81, 1–31.

Dini, A., Westerman, D.S., Innocenti, F., Rocchi, S., 2008a. Magma emplacement in a transfer zone: the Miocene mafic Orano dyke swarm of Elba Island, Tuscany, Italy. Geol. Soc. London. Spec. Publ. 302, 131–148.

Dini, A., Mazzarini, F., Musumeci, G., Rocchi, S., 2008b. Multiple hydro-fracturing by boron-rich fluids in the late Miocene contact aureole of eastern Elba Island (Tuscany, Italy). Terra Nova 20, 318–326.

Ducoux, M., Branquet, Y., Jolivet, L., Arbaret, L., Grasemann, B., Rabillard, A., Gumiaux, C., Drufin, S., 2017. Syn-kinematic skarns and fluid drainage along detachments: the West Cycladic Detachment System on Serifos Island (Cyclades, Greece) and its related mineralization. Tectonophysics 695, 1–26.

Dünkel, I., 2002. The genesis of East Elba iron ore deposits and their interrelation with Messinian Tectonics. Tuebinger Geowiss. Arb. Reihe A 65, 1–143.

Duranti, S., Palmeri, R., Pertusati, P.C., Ricci, C.A., 1992. Geological evolution and metamorphic petrology of the basal sequences of Eastern Elba (complex II). Acta Vulcanol. 2, 213–229.

Faulds, J.E., Hinz, N., Kreemer, C., Coolbaugh, M., 2012. Regional patterns of geothermal activity in the Great Basin region, western USA: Correlation with strain rates. Trans. Geothermal Resources Council 36 (2), 897–902.

Faulkner, D.R., Armitage, P.J., 2013. The effect of tectonic environment on permeability development around faults and in the brittle crust. Earth Planet. Sci. Lett. 375, 71–77.

Finetti, I., Boccaletti, M., Bonini, M., Del Ben, A., Geletti, R., Pipan, M., Sani, F., 2001. Crustal section based on CROP seismic data across the North Tyrrhenian-northern Apennines-Adriatic Sea. Tectonophysics 343, 135–163.

Franchini, M.B., de Barrio, R.E., Pons, M.J., Schalamuk, I.B., Rios, F.J., Meinert, L., 2007. Fe Skarn, Iron Oxide Cu-au, and Manto Cu-(Ag) deposits in the Andes Cordillera of Southwest Mendoza Province (34°–36°S), Argentina. Explor. Min. Geol. 16, 233–265.

Frezzotti, M.L., Tecce, F., Casagli, A., 2012. Raman spectroscopy for fluid inclusion analysis. J. Geochem. Explor. 112, 1–20.

Gagnevin, D., Daly, J.S., Horstwood, M.S.A., Whitehouse, M.J., 2011. In-situ zircon U-Pb, oxygen and hafnium isotopic evidence for magma mixing and mantle metasomatism in the Tuscan Magmatic Province, Italy. Earth Planet. Sci. Lett. 305 (1–2), 45–56.

Garfagnoli, F., Menna, F., Pandeli, E., Principi, G., 2005. The Porto Azzurro Unit (Mt. Calamita promontory, South-Eastern Elba Island, Tuscany): stratigraphic, tectonic and metamorphic evolution. Ital. J. Geosci. 3, 119–138.

Garofalo, P.S., Maffei, J., Papeschi, S., Dellisanti, F., Neff, C., Schwarz, G., Schmidt, P.K., Günther, D., 2023. Fluid-rock interaction, skarn genesis, and hydrothermal alteration within an upper crustal fault zone (Island of Elba, Italy). Ore Geol. Rev. 154, 105348 https://doi.org/10.1016/j.oregeorev.2023.105348.

Gianelli, G., Ruggieri, G., 2002. Evidence of a contact metamorphic aureole with high temperature metasomatism in the deepest part of the active geothermal field of Larderello. Italy. Geothermics 31, 443–474.

Gibbs, A.D., 1990. Linked faults in basin formation. J. Struct. Geol. 12, 795–803.

Gillespie, P.A., Johnston, J.D., Loriga, M.A., McCaffrey, K.J.W., Walsh, J.J., Watterson, J., 1999. Influence of layering on vein systematics in line samples. In: McCaffrey, K.J.W., Lonergan, L., Wilkinson, J.J. (Eds.), Fractures, Fluid Flow and Mineralisation, vol. 155. Geological Society London, Special Publication, pp. 35–56.

Goldstein, R.H., 2003. Petrographic Analysis of Fluid Inclusions. Chapter in Book Fluid Inclusions: Analysis and Interpretation. Edition: Short Course 32. Mineralogical Association of Canada, pp. 9–53.

Goldstein, R.H., Reynolds, T.J., 1994. Systematics of Fluid Inclusions in Diagenetic Minerals: SEPM Short Course 31. Society for Sedimentary Geology, p. 199.

Haynes, F.M., 1985. Determination of fluid inclusions composition by sequential freezing. Econ. Geol. 80, 1436–1439.

Haynes, F.M., Sterner, S.M., Bodnar, R.J., 1988. Synthetic fluid inclusions in natural quartz. IV. Chemical analyses of fluid inclusions by SEM/EDA: evaluation of method. Geochim. Cosmochim. Acta 52 (5), 969–977.

Hedenquist, J.W., Henley, R.W., 1985. The importance of CO_2 on freezing point measurements of fluid inclusions; evidence from active geothermal systems and implications for epithermal ore deposition. Econ. Geol. 80, 1379–1406.

Hedenquist, J.W., Lowenstern, J.B., 1994. The role of magmas in the formation of hydrothermal ore deposits. Nature 370, 519–527.

Heinrich, C.A., Bain, J.H.C., Mernagh, T.P., Wyborn, L.A.I., Andrew, A.S., Waring, C.L., 1995. Fluid and mass transfer during metabasalt alteration and copper mineralization at Mount Isa, Australia. Econ. Geol. 90 (4), 705–730. https://doi.org/10.2113/gsecongeo.90.4.705.

Keller, J.V.A., Pialli, G., 1990. Tectonics of the island of Elba: a reappraisal. Ital. J. Geosci. 109 (2), 413–425.

Kontak, D.J., 2004. Analysis of evaporate mounds as complement to fluid-inclusion thermometric data: case studies from granitic environments in Nova Scotia and Peru. Can. Mineral. 42, 1315–1329.

Lecumberri-Sanchez, P., Steele-MacInnis, M., Bodnar, R.J., 2015. Synthetic fluid inclusions XIX. Experimental determination of the vapor-saturated liquidus of the system H_2O–NaCl–$FeCl_2$. Geochim. Cosmochim. Acta 148, 34–49.

Liotta, D., 1991. The Arbia-Val Marecchia Line, Northern Apennines. Eclogae Geol. Helv. 84, 413–430.

Liotta, D., Brogi, A., 2020. Pliocene-Quaternary fault kinematics in the Larderello geothermal area (Italy): Insights for the interpretation of the present stress field. Geothermics 83. https://doi.org/10.1016/j.geothermics.2019.101714.

Liotta, D., Ruggieri, G., Brogi, A., Fulignati, P., Dini, A., Nardini, I., 2010. Migration of geothermal fluids in extensional terrains: the ore deposits of the Boccheggiano-Montieri area (southern Tuscany, Italy). Int. J. Earth Sci. 99, 623–644.

Liotta, D., Brogi, A., Meccheri, M., Dini, A., Bianco, C., Ruggieri, G., 2015. Coexistence of low-angle normal and high-angle strike- to oblique-slip faults during late Miocene mineralization in eastern Elba Island (Italy). Tectonophysics 660, 17–34.

Liotta, D., Brogi, A., Ruggieri, G., Rimondi, V., Zucchi, M., Helgadóttir, H.M., Montegrossi, G., Friðleifsson, G.O., 2020. Fracture analysis, hydrothermal mineralization and fluid pathways in the Neogene Geitafell central volcano: insights for the Krafla active geothermal system, Iceland. J. Volcanol. Geotherm. Res. 391, 106502 https://doi.org/10.1016/j.jvolgeores.2018.11.023.

Liotta, D., Brogi, A., Ruggieri, G., Zucchi, M., 2021. Fossil vs. active Geothermal Systems: A Field and Laboratory Method to Disclose the Relationships between Geothermal Fluid Flow and Geological Structures at Depth. Energies 14, 933. https://doi.org/10.3390/en14040933.

Lippolt, H., Wernicke, R., Bahr, R., 1995. Paragenetic specularite and adularia (Elba, Italy) - Concordant (U + Th)-he and K-Ar ages. Earth Planet. Sci. Lett. 132, 43–51.

Lister, G.S., Etheridge, M.A., Symonds, P.A., 1986. Detachment faulting and the evolution of passive continental margins. Geology 14, 246–250.

Locardi, E., Nicolich, R., 1992. Geodinamica del Tirreno e dell'Appennino centro-meridionale: la nuova carta della Moho. Mem. Soc. Geol. Ital. 41, 121–140.

Lugli, S., 2001. Timing of post-depositional events in the Burano Formation of the Secchia Valley (Upper Triassic, northern Apennines), clues from gypsum–anhydrite transitions and carbonate metasomatism. Sediment. Geol. 140, 107–122.

Maineri, C., Benvenuti, M., Costagliola, P., Dini, A., Lattanzi, P., Ruggieri, G., Villa, I., 2003. Sericitic alteration at the La Crocetta deposit (Elba Island, Italy): interplay between magmatism, tectonics and hydrothermal activity. Mineral. Deposita 38, 67–86.

Martinis, B., Pieri, M., 1964. Alcune notizie sulla formazione evaporitica del Triassico nell'Italia centrale e meridionale. Mem. Soc. Geol. Ital. 4, 649–678.

Matera, P., Ventruti, G., Zucchi, M., Brogi, A., Capezzuoli, E., Liotta, D., Yu, T.-L., Shen, C.-C., Huntington, K.W., Rinyu, L., Kele, S., 2021. Geothermal Fluid Variation Recorded by Banded Ca-Carbonate Veins in a Fault-Related, Fissure Ridge-Type Travertine Depositional System (Iano, southern Tuscany, Italy). Geofluids 8817487.

Moeller, S., Grevemeyer, I., Ranero, C.R., Berndt, C., Klaeschen, D., Sallares, V., Zitellini, N., De Franco, R., 2013. Early-stage rifting of the northern Tyrrhenian Sea Basin: results from a combined wide-angle and multichannel seismic study. Geochem. Geophys. Geosyst. 14, 3032–3052. https://doi.org/10.1002/ggge.20180.

Molli, G., 2008. Northern Apennines Corsica orogenic system: an updated overview. J. Geol. Soc. Spec. Publ. 298, 413–442. https://doi.org/10.1144/SP298.19.

Monastero, F.C., Katzenstein, A.M., Miller, J.S., Unruh, J.R., Adams, M.C., Richargd-Dinger, K., 2005. The Coso geothermal field: a nascent metamorphic core complex. GSA Bull. 117, 1534–1553.

Montecatini, 1950–1953. Colonne stratigrafiche dei sondaggi di ricerca per pirite e ferro perforati presso le miniere di Terranera e Ortano all'Isola d'Elba. Rapporto interno Rimin S.p.A., Aquater S.p.A. San Lorenzo in Campo. Available at. https://www.pconti.net/phpSearch.php.

Musumeci, G., Mazzarini, F., Cruden, A.R., 2015. The Zuccale Fault, Elba Island Italy: a new perspective from fault architecture. Tectonics 34, 1195–1218. https://doi.org/10.1002/2014TC003809.

Nabelek, P.I., Labotka, T.C., 1993. Implications of geochemical fronts in the Notch Peak contact-metamorphic aureole, Utah, USA. Earth Planet. Sci. Lett. 119, 539–559.

Orlando, A., Ruggieri, G., Chiarantini, L., Montegrossi, G., Rimondi, V., 2017. Experimental investigation of biotite-rich schist reacting with B-bearing fluids at upper crustal conditions and correlated tourmaline formation. Minerals 7, 155. https://doi.org/10.3390/min7090155.

Papeschi, S., Musumeci, G., Massonne, H.-J., Mazzarini, F., Ryan, E.J., Viola, G., 2020. High-P ($P = 1.5–1.8$ GPa) blueschist from Elba: Implications for underthrusting and exhumation of continental units in the Northern Apennines. J. Metamorph. Geol. 38 (5), 495–525.

Passchier, C.W., Trouw, R.A.J., 2005. Microtectonics, 2nd ed. Springer Science and Business Media, p. 384.

Peccerillo, A., 2003. Plio-quaternary magmatism in Italy. Episodes 26, 222–226.

Pérez-Flores, P., Cembrano, J., Sánchez-Alfaro, P., Veloso, E., Arancibia, G., Roquer, T., 2016. Tectonics, magmatism and paleo-fluid distribution in a strike-slip setting: Insights from the northern termination of the Liquiñe–Ofqui fault System, Chile. Tectonophysics 680 (12), 192–210. https://doi.org/10.1016/j.tecto.2016.05.016.

Pertusati, P.C., Raggi, G., Ricci, C.A., Duranti, S., Palmeri, R., 1993. Evoluzione post-collisionale dell'Elba centro-orientale. Mem. Soc. Geol. Ital. 49, 297–312.

Pope, E.C., Bird, D.K., Arnórsson, S., 2014. Stable isotopes of hydrothermal minerals as tracers for geothermal fluids in Iceland. Geothermics 49, 99–110.

Pope, E.C., Bird, D.K., Arnórsson, S., Giroud, N., 2016. Hydrology of the Krafla geothermal system, Northeast Iceland. Geofluids 16, 175–197.

Rocchi, S., Westerman, D.S., Dini, A., Innocenti, F., Tonarini, S., 2002. Two-stage laccolith growth at Elba Island (Italy). Geology 30, 983–986.

Rocchi, S., Westerman, D.S., Dini, A., Farina, F., 2010. Intrusive sheets and sheeted intrusions at Elba Island (Italy). Geosphere 6, 225–236. https://doi.org/10.1130/GES00551.1.

Roedder, E., 1984. Fluid inclusions. Mineralogical Society of America. Rev. Mineral. 12, 644.

Romagnoli, P., Arias, A., Barelli, A., Cei, M., Casini, M., 2010. An updated numerical model of the Larderello-Travale geothermal system, Italy. Geothermics 39, 292–313.

Rossetti, F., Tecce, F., Billi, A., Brilli, M., 2007. Patterns of fluid flow in the contact aureole of the late Miocene Monte Capanne pluton (Elba Island, Italy): the role of structures and rheology. Contrib. Mineral. Petrol. 153, 743–760.

Rossetti, F., Glodny, J., Theye, T., Maggi, M., 2015. Pressure–temperature–deformation–time of the ductile Alpine shearing in Corsica: from orogenic construction to collapse. Lithos 218–219, 99–116.

Rowland, J.V., Sibson, R.H., 2004. Structural controls on hydrothermal flow in a segmented rift system Taupo Volcanic Zone, New Zealand. Geofluids 4, 259–283.

Ruggieri, G., Gianelli, G., 1999. Multi-stage fluid circulation in a hydraulic fracture breccia of the Larderello geothermal field Italy. J. Volcanol. Geotherm. Res. 90, 241–261.

Ryan, E., Papeschi, S., Viola, G., Musumeci, G., Mazzarini, F., Torgersen, E., Sørensen, B. E., Ganerød, M., 2021. Syn-Orogenic Exhumation of High-P units by Upward Extrusion in an Accretionary Wedge: Insights from the Eastern Elba Nappe Stack (Northern Apennines, Italy). Tectonics 40 (5). https://doi.org/10.1029/2020tc006348.

Samson, I.M., Williams-Jones, A.E., Ault, K.M., Gagnon, J.E., Fryer, B.J., 2008. Source of fluids forming distal Zn-Pb-Ag skarns: evidence from laser ablation-inductively coupled plasma-mass spectrometry analysis of fluid inclusions from El Mochito, Honduras. Geology 36, 947–950.

Saupé, F., Marignac, C., Moine, B., Sonet, J., Zimmermann, J.L., 1982. Datation par les methodes K/Ar et Rb/Sr de quelques roches de la partie orientale de l'Ile d'Elbe (Province de Livourne, Italie). Bull. Mineral. 105, 236–245.

Serri, G., Innocenti, F., Manetti, P., 1993. Geochemical and petrological evidence of the subduction of delaminated Adriatic continental lithosphere in the genesis of the Neogene-Quaternary magmatism of Central Italy. Tectonophysics 223, 117–214.

Shepherd, T.J., Rankin, A.H., Alderton, D.H.M., 1985. A Practical Guide to Fluid Inclusion Studies. Blackie and Son Ltd, Glasgow, pp. 1–239.

Sibson, R.H., 1981. Fluid flow accompanying faulting: Field evidence and models. In: Simpson, D.W., Richards, P.G. (Eds.), Earthquake Prediction: An International Review. American Geophysical Union, Maurice Ewing Series, vol. 4, pp. 593–603.

Sibson, R.H., 1987. Earthquake rupturing as a mineralising agent in hydrothermal systems. Geology 15, 701–704.

Sibson, R.H., 1990. Conditions for fault-valve behaviour. In: Knipe, E.H., Rutter, E.H. (Eds.), Deformation Mechanisms, Rheology and Tectonics, 54. Geological Society, pp. 15–28.

Sibson, R.H., 2000. Fluid involvement in normal faulting. J. Geodyn. 29, 469–499. https://doi.org/10.1016/S0264-3707(99)00042-3.

Sibson, R.H., Roberts, F., Poulsen, K.H., 1988. High angle reverse fault, fluid pressure cycling and mesothermal gold quartz deposits. Geology 16, 551–555.

Smith, M.P., Banks, D.A., Yardley, B.W.D., Boyce, A., 1996. Fluid inclusion and stable isotope constraints on the genesis of the Cligga Head Sn-W deposit, S.W. England. Eur. J. Mineral. 8, 961–974.

Smith, S.A.F., Holdsworth, R.E., Collettini, C., Imber, J., 2007. Using footwall structures to constrain the evolution of low-angle normal faults. Geol. Soc. Lond. J. 164, 1187–1192. https://doi.org/10.1144/0016-76492007-009.

Smith, S.A.F., Holdsworth, R.E., Collettini, C., 2011. Interactions between low-angle normal faults and plutonism in the upper crust: insights from the Island of Elba, Italy. GSA Bull. 123, 329–346.

Spiess, R., Langone, A., Caggianelli, A., Stuart, F.M., Zucchi, M., Bianco, C., Brogi, A., Liotta, D., 2021. Unveiling ductile deformation during fast exhumation of a granitic pluton in a transfer zone. J. Struct. Geol. 147, 104326 https://doi.org/10.1016/j.jsg.2021.104326.

Spiess, R., Langone, A., Caggianelli, A., Stuart, F.M., Zucchi, M., Bianco, C., Brogi, A., Liotta, D., 2022. Reply to Mazzarini et al. Comment on "Unveiling ductile deformation during fast exhumation of a granitic pluton in a transfer zone". J. Struct. Geol. 155, 104498 https://doi.org/10.1016/j.jsg.2021.104498.

Spina, A., Capezzuoli, E., Brogi, A., Cirilli, S., Liotta, D., 2019. Middle-late Permian microfloristic evidences in the metamorphic successions of Northern Apennines: insights for age constraining and palaeo-geographic correlations. J. Geol. Soc. Lond. https://doi.org/10.1144/jgs2018-202.

Steele-MacInnis, M., 2018. Fluid inclusions in the system H_2O-NaCl-CO_2: an algorithm to determine composition, density and isochore. Chem. Geol. 498, 31–44. https://doi.org/10.1016/j.chemgeo.2018.08.022.

Steele-MacInnis, M., Bodnar, R.J., Naden, J., 2011. Numerical model to determine the composition of H_2O-NaCl-$CaCl_2$ fluid inclusions based on microthermometric and microanalytical data. Geochim. Cosmochim. Acta 75 (1), 21–40.

Steele-MacInnis, M., Lecumberri-Sanchez, P., Bodnar, R.J., 2012. HOKIEFLINCS_H_2O-NACL: a Microsoft Excel spreadsheet for interpreting microthermometric data from fluid inclusions based on the PVTX properties of H_2O-NaCl. Comput. Geosci. 49, 334–337.

Steele-MacInnis, M., Ridley, J., Lecumberry-Snachez, P., Schlegel, T.U., Heinrich, C.A., 2016. Application of low-temperature microthermometric data for interpreting multicomponent fluid inclusion compositions. Earth Sci. Rev. 159, 14–35. https://doi.org/10.1016/j.earscirev.2016.04.011.

Tanelli, G., Benvenuti, M., Costagliola, P., Dini, A., Lattanzi, P., Manieri, C., Mascaro, I., Ruggieri, G., 2001. The iron mineral deposits of Elba Island: state of the art. Ofioliti 26, 239–248.

Uysal, I.T., Feng, Y., Zhao, J., Isik, V., Nuriel, P., Golding, S., 2009. Hydrothermal CO_2 degassing in seismically active zones during the late Quaternary. Chem. Geol. 265, 442–454.

Vai, G.B., Martini, I.P., 2001. Anatomy of an Orogen: The Apennines and Adjacent Mediterranean Basins. Kluwer Academic, Dordrecht, pp. 15–31.

Vezzoni, S., Dini, A., Rocchi, S., 2016. Reverse telescoping in a distal skarn system (Campiglia Marittima, Italy). Ore Geol. Rev. 77, 176–193. https://doi.org/10.1016/j.oregeorev.2016.03.001.

Viola, G., Torgersen, E., Mazzarini, F., Musumeci, G., van der Lelij, R., Scho Nenberger, J., Garofalo, P.S., 2018. New constraints on the evolution of the inner Northern Apennines by K-Ar dating of late Miocene-early Pliocene compression on the Island of Elba, Italy. Tectonics 37 (9), 3229–3243.

Viola, G., Musumeci, G., Mazzarini, F., Tavazzani, L., Curzi, M., Torgersen, E., Van Der Lelij, R., Aldega, L., 2022. Structural characterization and K-Ar illite dating of reactivated, complex and heterogeneous fault zones: lessons from the Zuccale Fault, Northern Apennines. Solid Earth 13 (8), 1327–1351.

Viti, C., Brogi, A., Liotta, D., Mugnaioli, E., Spiess, R., Dini, A., Zucchi, M., Vannuccini, G., 2016. Seismic slip recorded in tourmaline fault mirrors from Elba Island (Italy). J. Struct. Geol. 86, 1–12.

Westerman, D.S., Dini, A., Innocenti, F., Rocchi, S., 2004. Rise and fall of a nested Christmas-tree laccolith complex, Elba Island, Italy. In: Breitkreuz, C., Petford, N. (Eds.), Physical Geology of High- Level Magmatic Systems, Geological Society, 234. Special Publication, London, pp. 195–213.

Whitney, D.L., Evans, B.W., 2010. Abbreviations for names of rock-forming minerals. Am. Mineral. 95, 185–187.

Wu, L.-Y., Stuart, F.M., Di Nicola, L., Heizler, M., Benvenuti, M., Hu, R.-Z., 2019. Multi-aliquot method for determining (U + Th)/he ages of hydrothermal hematite: Returning to Elba. Chem. Geol. 504, 151–157.

Yano, Y., Ishido, T., 1996. Numerical investigation of pressure transient responses of a well penetrating a deep geothermal reservoir at super-critical conditions, proceedings. In: Twenty-First Workshop on Geothermal Reservoir Engineering. Stanford University, Stanford. California (January 22–24. SGP-TR-151).

Yardley, B.W.D., 2005. Metal concentrations in crustal fluids and their relationship to ore formation. Econ. Geol. 100, 613–632.

Yardley, B.W.D., Bodnar, R.J., 2014. Fluids in the Continental Crust. Geochemical Perspectives 3 (1), 127.

Zucchi, M., 2020. Faults controlling geothermal fluid flow in low permeability rock volumes: an example from the exhumed geothermal system of eastern Elba Island (northern Tyrrhenian Sea, Italy). Geothermics 85, 101765. https://doi.org/10.1016/j.geothermics.2019 (101765).

Zucchi, M., Brogi, A., Liotta, D., Rimondi, V., Ruggieri, G., Montegrossi, G., Caggianelli, A., Dini, A., 2017. Permeability and hydraulic conductivity of faulted micaschist in the eastern Elba Island exhumed geothermal system (Tyrrhenian Sea, Italy): insights from Cala Stagnone. Geothermics 70, 125–145.

Zucchi, M., Brogi, A., Liotta, D., Caggianelli, A., Dini, A., Ventruti, G., Ruggieri, G., Matera, P.F., 2022. Fractures, fluid flow and inherited structures in geothermal systems: inputs from the Fe-ore deposits of eastern Elba Island (Northern Apennines, Italy). Geol. Mag. 1–24 https://doi.org/10.1017/S0016756822000310.